Mitotic slippage causes nuclear instability in polyploid cells

Gemble S[1,*], Budzyk M[1], Simon A[1], Lambuta R[2,3], Weiss N[4], Forest A[4], Miroshnikova YA[5], Scotto Di Carlo F[1], Marthiens V[1], Verdel C[1], Fang J[6,7], Desdouets C[6,7], Wickström SA[8,9], Ciriello G[10], Oricchio E[2], Almouzni G[4] & Basto R[1,*].

Author affiliations

1. Biology of Centrosomes and Genetic Instability, Institut Curie, Centre National de la Recherche Scientifique (CNRS), Unité Mixte de Recherche 144, Université Paris Sciences et Lettres (PSL Research University), Paris, France.
2. Swiss Institute for Experimental Cancer Research (ISREC), School of Life Sciences, EPFL, Switzerland
3. Present address: Institute of Molecular Biology, Mainz, Germany
4. Chromatin dynamics, Institut Curie, Centre National de la Recherche Scientifique (CNRS) Unité Mixte de Recherche 3664, Université Paris Sciences et Lettres (PSL Research University), University, Sorbonne Université, Paris, France
5. Max Planck Research Group Biophysical Regulation of Cell State Dynamics, Max Planck Institute for Molecular Biomedicine, 48149 Münster, Germany.
6. Centre de Recherche des Cordeliers, Sorbonne Université, INSERM, Université de Paris, Paris, France.
7. Genomic Instability, Metabolism, Immunity and Liver Tumorigenesis laboratory, Equipe Labellisée LIGUE 2023, Paris, France.
8. Department of Cell and Tissue Dynamics, Max Planck Institute for Molecular Biomedicine, 48149 Münster, Germany.
9. Stem Cells and Metabolism Research Program, Faculty of Medicine, University of Helsinki, 00290 Helsinki Finland.
10. Department of Computational Biology, University of Lausanne (UNIL), Switzerland.

* Corresponding author: renata.basto@curie.fr and simon.gemble@curie.fr

Contact information

Correspondence: renata.basto@curie.fr and simon.gemble@curie.fr

Abstract

Whole-genome duplication (WGD), leading to polyploidy, can arise in physiological and pathological contexts[1–5]. WGD can occur via non-canonical cell cycles such as mitotic slippage, cytokinesis failure or endoreplication[1,3]. However, whether the route of WGD shapes the behaviour of the resulting polyploid cells remains unclear. Here, we compared these routes under both physiological and non-physiological conditions. Remarkably, only mitotic slippage led to widespread nuclear abnormalities defined by highly variable nuclear deformations that we termed nuclear instability. These nuclei were softer and more vulnerable to microtubule-driven deformations leading to invaginations. Mechanistically, we found defects in chromatin compaction and H3K9me2 chromatin-lamina interactions. Moreover, transcriptional stability was disrupted as early as G1, with effects intensifying by G2. Importantly, we observed similar nuclear instability in megakaryocytes, which are physiological polyploid cells that we demonstrate here to be generated by mitotic slippage, providing a potential explanation for their atypical nuclear architecture[6,7]. In striking contrast, nuclear shape was stable in different physiological polyploid cells generated by cytokinesis failure and endoreplication. Overall, our findings highlight that the path to polyploidy matters and that mitotic slippage uniquely destabilizes nuclear architecture and gene expression, with implications for both physiology and disease.

Keywords

Whole Genome Duplication- Polyploidy - Nuclear Architecture - Genome Organization - Mitotic slippage - Nuclear lamins - H3K9me2 - H3S10.

Introduction

Most animal cells are diploid, carrying two copies of each chromosome (2N). Through a developmentally regulated and reproducible program, certain cells increase their chromosome number through whole genome duplication (WGD), accumulating multiple sets of each chromosome (> 2N) – hereafter called physiological polyploidy[9]. In most cases, the increase in DNA content is related with an increase in metabolic activity, barrier function or even regenerative capacity. For instance, in mammals, megakaryocytes become polyploid (modal ploidy 16N) to increase their metabolic capacity and produce a high number of platelets[7,10] while salivary gland cells become polyploid (1024N) during *Drosophila* larval development to produce large quantities of glue, which is necessary for *Drosophila* pupation[9,11,12]. Mammalian hepatocytes also become polyploid (8N) during liver maturation. The role of polyploidy in this context is still debated, but studies suggest that polyploid hepatocytes may have higher metabolic and regenerative capacities[8,13]. In contrast, when WGD occurs in cells that should not become polyploid - hereafter called unscheduled polyploidy - it leads to genetic and chromosomal instability[2,14–20]. For example, tetraploidy (4N) - that results from a single WGD - is a common feature of human tumours. Indeed, about 30% of tumours are tetraploid, reaching up to 70% in some specific cases like non-small cell lung carcinomas[4,5,18,21].

The canonical cell cycle typical of somatic cells relies on coupling genome duplication with mitotic cell division to generate two diploid daughter cells[22]. Polyploid cells can be generated by alternative cell cycles - hereafter called non-canonical cell cycles. These cell cycles rely on incomplete or absent mitosis uncoupling the duplication of the genome from cell division leading thus to WGD[1]. Cells can exit mitosis before or after chromosome segregation through mitotic slippage (MS) or cytokinesis failure (CF), respectively (Figure 1A). Alternatively, cells can alternate S-phase with G-phase using a cell cycle called endoreplication (EnR) (Figure 1A). MS and EnR generate polyploid cells with a single nucleus, while CF generates binucleated polyploid cells[6,12,23]. However, the functional consequences of these non-canonical cell cycles remain poorly understood. Indeed, while MS, CF and EnR have been proposed to take place in physiological and pathological contexts[1,2,9,13,24], it is still not clear whether different means to induce WGD lead to different outcomes.

Here, by combining comparative analyses integrating physiological and unscheduled models of WGD, we found that MS unlike CF and EnR, generates polyploid cells with irregular nuclear architecture. Mechanistically, we identified that MS leads to mitotic exit with high levels of histone 3 phosphorylation on serine 10 (H3S10). This impairs nuclear envelope reformation compromising nuclear stiffness allowing the microtubules to promote nuclear deformability. Our findings shows that low H3S10 phosphorylation at mitotic exit is a pre-requisite to rebuild functional chromatin-Lamina network interactions. This induces changes in chromatin states, in 3D genome organization and in gene expression programs. Importantly, we observed that a similar mechanism contributes to the irregular nuclear shape of the megakaryocytes, physiological polyploid cells generated by MS. Overall, these data highlight the fact that different means to generate WGD have different outcomes, which may influence downstream cell functions.

Results

Unscheduled WGD induced through MS generates cells with nuclear instability

To define whether different routes of WGD have different outcomes, we induced unscheduled WGD through mitotic slippage (MS), cytokinesis failure (CF) or endoreplication (EnR) in RPE-1 cells (see methods, Figure 1A and Supp. Fig. 1A)[15,25], which are p53-proficient diploid human cell line. As previously described and due to the methods employed to induce WGD[15], this strategy generates a mixed population of diploid (2N) and tetraploid (4N) cells that can be distinguished by nuclear and cell size[15]. Importantly, to avoid any effect due to cell cycle progression, cells were synchronised in the first G1 upon WGD using the CDK4/6 inhibitor Palbociclib at 1µM (see methods).

Using these highly comparable systems, we observed that MS, but not CF and EnR, generated tetraploid cells with abnormal nuclear shape (Fig. 1B). To quantitatively analyse the nuclear architecture in these cells, we measured nuclear circularity and solidity, two indices, informing on nuclear elongation and on the presence of nuclear invaginations, respectively (see methods, Fig. 1C). We observed that tetraploid cells generated through MS showed decreased nuclear circularity and solidity, while CF and EnR showed values similar to diploid cells (Fig. 1C-E). Similar results were obtained using alternative methods and other diploid cell lines - BJ and HCT116 (see methods and Supp. Fig. 1A-H). Additionally, when cells were cultured in 3D, nuclear deformations upon MS were still detected (see methods and Supp. Fig. 1I-L). Inducing MS in asynchronous cells, also showed similar results (see methods and Supp. Fig. 1M). Interestingly, we found that the nuclear area was similar in MS- and EnR-generated newly born tetraploid cells (Supp. Fig. 1N-O), suggesting that nuclear defects upon MS does not affect the overall nuclear size but only nuclear architecture.

We next performed live imaging approaches using cells stably expressing mCherry-H2B, to follow the transition from G2 to the subsequent G1 at the single cell level. In control diploid cells that undergo canonical mitotic divisions, nuclear circularity and solidity from G2 to G1 remained stable (Fig. 1F-H and Movie 1). In contrast, in tetraploid cells generated by MS an obvious decrease could be noticed (Fig. 1F-H and Movie 2). Plotting the delta circularity (defined as the difference

between nuclear circularity in G2 vs in G1) showed values close to 0 in diploid cells (Fig. 1I). This indicates that nuclear architecture was similar before and after mitosis in diploid cells - i.e. nuclear architecture was stable over subsequent cell cycles, as expected. In MS-induced tetraploid cells however, the delta circularity was increased (Fig. 1I), indicating that MS impairs the re-establishment of nuclear architecture in newly born tetraploid cells. Indeed, we observed that MS-induced tetraploid G1 cells exhibited heterogenous nuclear shapes (Fig. 1J), that were still present in the following G2 (Supp Fig. 1P). Moreover, at the population level, we were struck by the level of heterogenous nuclear shapes. This reflects that WGD when induced through MS generates a high degree of nuclear shape diversity that seems stochastic - a phenomenon that we called here nuclear instability. In contrast, diploid, CF- and EnR-generated tetraploid cells exhibited similar and homogenous nuclear shapes (Fig. 1J).

To understand whether these abnormal shapes were maintained over multiple cell cycles, we induced MS in a p53-depleted RPE-1 cell line, which is permissive to tetraploid cell proliferation[15,26–28]. Surprisingly, we observed that nuclear circularity and solidity remained low over multiple cell cycles in MS-generated tetraploid cells (Supp Fig. 1Q-S).

Together, these findings show that MS generates nuclear instability - i.e. a high degree of nuclear shape diversity. In striking contrast, CF and EnR induction results in homogenous nuclear morphologies.

Mitotic slippage generates softer tetraploid nuclei

We then investigated the mechanism underlying nuclear deformations upon MS. To identify the origins of the nuclear deformability characteristic of MS-induced tetraploid cells, we conducted a mini-screen in which both chromatin and nuclear envelope components were visually examined using structural illumination microscopy. The candidate list was compiled based on their well-established roles in nuclear morphology[29–35]. We qualitatively and quantitatively ascertained the localization of 10 nuclear envelope components and 9 histone marks. The fluorescence intensity levels were measured in diploid and tetraploid G1 cells at the level of the whole nucleus and at the nuclear envelope. In addition, we also measured fluorescence intensity at intact and deformed nuclear envelope regions (see methods and Supp. Fig. 2A-E).

We noticed a global increase in H3K9ac and H3K27ac (Supp. Fig. 2D and F). These chromatin marks are commonly associated with open chromatin/euchromatin[36]. Interestingly, we also found a decrease in the number of Heterochromatin Protein 1 (HP1) foci, usually associated with closed chromatin/heterochromatin[37,38] (Supp. Fig. 2G). Together, these findings suggest that MS impairs chromatin states in newly born tetraploid cells.

It is well established that several factors, including chromatin states, contribute significantly to nuclear envelope deformability counteracting cytoplasmic forces that act on the nucleus[29,30]. It is therefore possible that the nuclear deformations of tetraploid cells induced through MS reflected a decrease in nuclear mechanical properties due to changes in chromatin compaction. To test this possibility, we first investigated whether MS alters nuclear stiffness using atomic force microscopy (AFM) (Fig 2A). Using two different strategies to generate MS, we found that tetraploid nuclei were significantly softer than their diploid counterparts (Fig. 2A-C and Supp. Fig. 3A). We then studied the functional relationship between higher acetylation levels, decreased nuclear stiffness and nuclear deformations upon MS. We treated cells with C646, a histone acetylase inhibitor[39], which decreases histone acetylation levels promoting nuclear compaction (Supp. Fig. 3B-D) and resistance[40]. Strikingly, this was sufficient to prevent nuclear deformations upon MS (Supp. Fig. 3E).

Our data suggest that MS generates tetraploid cells with high levels of chromatin acetylation that contribute to decrease their nuclear stiffness promoting most likely nuclear deformability.

Microtubules contribute to nuclear deformations in tetraploid cells

Detailed analysis of mitotic exit in diploid and MS-induced tetraploid cells revealed an increase in nuclear area, most likely due to chromosome decondensation[41]. However, in tetraploid cells, this was accompanied by appearance of nuclear invaginations (Supp. Fig 3F, pink arrow). Indeed, while quantifying nuclear circularity and solidity, we found that these indices were quite stable in diploid cells during early G1 (Supp. Fig 3G, upper panel), whereas both parameters decreased in newly born tetraploid cells during mitotic exit (Supp. Fig 3G, lower panel). We thus hypothesised

that external forces could generate nuclear invaginations, promoted by the reduced nuclear stiffness we observed in MS-induced tetraploid cells (Fig. 2A-C).

Cytoskeleton components interact with the nuclear envelope, a process that contributes to the establishment of nuclear architecture[42]. Characterization of cytoskeleton proteins in G1 cells showed that microtubules (but not actin) accumulated at nuclear invaginations in MS-induced tetraploid cells (Supp. Fig 3H-K), which was not seen in EnR-generated tetraploid cells (Supp. Fig. 3L). Using time-lapse microscopy in cells incubated with SPY-tubulin and SPY-Actin, we followed microtubules and actin, respectively. We found that just after nuclear envelope reformation upon MS, microtubules accumulate at invagination sites assembling in thick bundles (Supp. Fig. 3M and Movie 3) whereas actin did not (Supp. Fig. 4A and Movie 4). These data suggest that microtubules unlike actin, contribute to nuclear instability in newly born tetraploid cells.

We also observed a significant decrease in Sun1 and Nesprin1 levels at the nuclear envelope (Supp. Fig. 2C-D). These proteins are part of the LInker of Nucleoskeleton and Cytoskeleton (LINC) complex and are associated with the inner and the outer nuclear envelope establishing the link between chromatin, the nuclear envelope and the cytoskeleton[34,42]. However, expressing a dominant negative KASH domain, known to inactivate the LINC complex, did not affect nuclear architecture upon MS (Supp. Fig. 4B-C). Further, we were unable to detect defects in the localization of the LINC complex in tetraploid MS cells induced through an alternative approach (Supp. Fig. 2E). These results suggest that even if members of the LINC complex are not correctly recruited to deformed nuclear areas, this complex does not seem to have a major role in generating nuclear deformations.

To functionally test the contribution of microtubules in generating nuclear invaginations, we removed microtubules using nocodazole, a microtubule-depolymerizing agent[43], just before MS (Supp. Fig. 4D and Movie 5-6). Strikingly, in the absence of microtubules, the nuclear shape in newly born tetraploid cells became more regular, presenting fewer deformations in G1, as also revealed by a decrease in the delta circularity (Supp. Fig. 4E). Moreover, treating tetraploid cells with nocodazole was sufficient to enhance both nuclear circularity and solidity (Supp. Fig. 4F-H). These data were confirmed using another mean to induce MS (Supp. Fig. 4I-K and Movie 7-8). Interestingly, removing microtubules in G1, a few hours after MS, did not improve the nuclear shape in newly born tetraploid cells (Supp. Fig. 4F-H). We

then tested whether stabilizing microtubules could exacerbate nuclear deformations. To do so, we treated tetraploid cells with low-doses of Taxol, a microtubule-stabilizing agent[44], before MS. In these conditions, nuclear deformations were even more impressive and a decrease in both nuclear circularity and solidity was noticed (Supp. Fig. 4L).

Our data show that the microtubule cytoskeleton is the main contributor to nuclear deformations in newly born tetraploid cells induced by unscheduled MS, and its action is limited to a short time window during mitotic exit.

Mitotic slippage impairs the interaction between chromatin and nuclear lamins

We next focused our study on H3K9me2 and H3.1/2 chromatin marks because their levels were decreased in specific regions that coincide with nuclear deformations in MS-induced tetraploid cells (Fig. 2D-E and Supp. Fig. 2D and Supp. Fig. 5A).These two marks are normally enriched at the nuclear periphery and associated with chromatin regions that are less dynamic[33,35]. Importantly, no changes in H3K9me3 levels upon MS (Supp. Fig. 2D and Supp. Fig. 5B), another mark associated with closed chromatin[35] were noticed. H3K9me2 coefficient of variation (CoV) at the nuclear envelope (defined as the ratio of the standard deviation to the mean) was increased in tetraploid cells (Fig. 2F), indicating uneven distribution of H3K9me2 in sharp contrast with the uniform distribution of H3K9me2 at the nuclear envelope of diploid nuclei (Fig. 2D-F). Similar defects in H3K9me2 localization at invaginations were found in tetraploid cells where MS was induced by a different mean, in BJ and in HCT116 cell lines (Supp. Fig. 5C-G).

Interestingly, we also observed a slight decrease in Lamin A/C intensity precisely at nuclear deformed regions (Fig. 2G-J and Supp. Fig. 5A). The Lamina, composed of a specific ratio of Lamin A/C and Lamin B proteins, plays a crucial role in maintaining nuclear architecture[30–32,45,46]. The loss of Lamin A/C was associated with an increase in Lamin B1 and Lamin B Receptor (LBR) levels (Fig. 2G-J and Supp. Fig. 3C). The ratio between Lamin A/C and B is crucial in establishing nuclear morphology[31,32,45,46]. Indeed, nuclear resistance is strongly impacted by Lamin A/C and a ratio dominated by Lamin B has thus been associated with soft tissues[45,46]. By measuring this ratio, we found differences in tetraploid cells at nuclear deformations regions. Frequently, Lamin B1 dominated the lamina network in invaginated domains,

while the levels of Lamin A/C were lower than the ones found in intact regions (Fig. 2I). Similar defects were observed in MS-generated tetraploid cells using an alternative method and in BJ and in HCT116 cell lines (Supp. Fig. 5C-G). In contrast, we found that both CF and EnR tetraploid cells displayed homogeneous distributions of H3K9me2 and Lamin ratios (Supp. Fig. 5H-K).

Together, our findings show that nuclei generated by MS display a regional decrease in H3K9me2 and Lamin A/C, which may be at the genesis of nuclear invaginations induced by the microtubule cytoskeleton (Fig. 2K).

Mitotic slippage allows mitotic exit with high H3 phosphorylation levels influencing nuclear morphology

During mitotic entry, phosphorylation of Ser10 of Histone 3 (H3S10) promotes chromatin dissociation from the lamina network facilitating nuclear envelope breakdown[33,47,48] (Fig. 3A-B). As cells exit mitosis, the phosphorylation levels gradually decrease allowing the re-establishment of chromatin/Lamin interactions and nuclear envelope reformation[33] (Fig. 3A-B). In contrast, MS leads to premature mitotic exit in a state characterized by high H3S10 phosphorylation levels (Fig. 3A-B).

To investigate whether mitotic exit with high H3S10 phosphorylation levels impact nuclear architecture, we inhibited Aurora B, a mitotic kinase contributing to H3S10 phosphorylation[49]. However, Aurora B inhibition induced MS[50] and nuclear deformations (Supp. Fig. 6A-B), most likely by affecting the phosphorylation of an Aurora B substrate involved in mitotic progression[51]. We thus decided to use a different and more targeted strategy. We generated a cell line, expressing an H3 mutant version, where Serine 10 was replaced by an Alanine residue - H3S10A[33], in the background of wild type (WT) H3. A partial decrease in H3S10 phosphorylation was noticed as expected (Supp. Fig. 6C). Importantly, this was sufficient to increase both nuclear circularity and solidity in newly born tetraploid MS-induced cells, improving their overall nuclear shape (Fig. 3C-E and Supp. Fig. 6E-F).

The levels of H3S10 phosphorylation are known to be influenced by the methylation status of the neighbouring lysine (H3K9). Indeed, high H3S10 phosphorylation levels are accompanied by low H3K9 methylation levels and vice versa, creating a “phospho/methyl switch”[33,52,53]. We found that this was also true in RPE-1 cells as expression of H3S10A (Supp. Fig. 6C), showed higher levels of

methylated H3K9 (Supp. Fig. 6D). Further, we used Methylstat, a demethylase inhibitor known to maintain high H3K9 methylation status[40], which resulted in a decrease in H3S10 phosphorylation levels in mitosis (Fig. 3F-I and Supp. 6G-H). Importantly, this prevents defects in H3K9me2 and Lamin A/C levels at the nuclear envelope and improve nuclear morphology upon MS (Fig.3J-N and Supp. Fig. 6I-L). This was also sufficient to prevent nuclear deformations by the microtubule cytoskeleton at mitotic exit upon MS even if thick microtubule bundles still accumulated around the nucleus (Fig. Supp. 7A and movie 9). These results were confirmed using another method to induce MS and in BJ and HCT116 cells (Supp. Fig. 6M-R). Interestingly, treating newly born tetraploid cells with Methylstat in G1, a few hours after MS, when H3S10 levels were low, did not restore or improve nuclear architecture in newly born tetraploid cells (Supp. Fig. 7B-E). This supports the idea that the status of chromatin at mitotic exit determines nuclear shape in a stable manner that cannot be reversed. Using additional chemical and genetic methods to increase H3K9 methylation prior to MS showed similar results (see methods and Supp. Fig. 7F-J). Further, as an alternative strategy to decrease H3S10 phosphorylation levels we blocked cells in mitosis for 12hrs before inducing MS. This was sufficient to decrease H3S10 phosphorylation and to improve nuclear shapes after MS (Supp. Fig. 7K-M). Finally, we inhibited the phosphatase responsible for H3S10 dephosphorylation at mitotic exit using Calyculin A[54] in diploid cells. This treatment resulted in increased H3S10 phosphorylation levels in diploid cells and remarkably, nuclear deformations characterized by invaginations with low H3K9me2 levels similar to those found in MS-generated tetraploid cells (Supp. Fig. 7N-O).

Together, our results show that low H3S10 phosphorylation at mitotic exit is a pre-requisite to rebuild functional chromatin-Lamina network interactions and thus to re-establish proper nuclear morphology and mechanics during nuclear re-assembly.

Mitotic slippage impairs 3D genome organisation and compaction and gene expression programs

We next investigated the functional consequences of nuclear deformations observed upon MS. Recently it has been shown that WGD in p53-deficient cells leads to loss of chromatin segregation explained by an increased proportion of contacts between chromosomes, compartments, and chromatin domains[55]. Insulation of topology

associated domains (TADs) requires a certain number of proteins that do not seem to scale with the tetraploid genome[55]. We wanted to investigate whether such defects were already detectable in the first G1 after MS. To do so, we isolated diploid and tetraploid cells using flow cytometry, as previously described[15] (Fig. 4A and Supp. Fig. 8A). Importantly, cell sorting did not affect nuclear deformations in MS-generated tetraploid cells (Supp. Fig. 8B). Using high throughput chromatin capture conformation (HiC), we compared interactions at the chromosomal level and between chromatin domains in diploid and newly born MS-generated tetraploid G1 cells. Similarly to what has been previously observed, we found an increased number of contacts between short and long chromosomes (Fig. 4B) and between A and B compartments (Supp. Fig. 8C-F) in tetraploid cells compared to diploid cells.

We next performed Chromatin Immunoprecipitation (ChIP) coupled with DNA sequencing to analyse the distribution of H3K9me2 and H3K9me3 in diploid and MS-tetraploid G1 cells. H3K9me2 and H3K9me3 are associated with heterochromatin and ensure transcriptional silencing necessary to maintain cell and tissue identity[56]. First, we observed that H3K9me2 and H3K9me3 enrichment at specific genomic regions was not altered upon MS (Fig. 4C-D). Nevertheless, analysis of H3K9me3 enrichment at the genome scale showed an increase in H3K9me3 levels upon MS (Fig. 4E and Supp Fig. 8G-I). This result was in contrast with the microscopy data (Supp Fig. 4B). However, H3K9me3 enrichment in tetraploid cells mostly localized in regions that were already enriched in this histone mark in diploid cells (red arrows, Fig. 4E), suggesting changes in H3K9me3 levels, but not in its distribution (Fig. 4E and Supp. Fig. 8I). In sharp contrast however, we observed that H3K9me2 levels globally increased in MS cells (Fig. 4F and Supp Fig. 8H-I), and importantly, in regions that were not necessarily occupied in diploid cells (green arrows, Fig. 4F). Interestingly, we also found that certain H3K9me2 enriched areas in diploid cells lost this distribution in MS cells (red arrows, Fig. 4F).

Our findings showing changes in genome organisation and chromatin state upon MS led us to test whether MS alters gene expression programs. We thus analysed newly born tetraploid cells in the first G1 or in the first G2 upon MS by RNAseq. We found that the further cells progressed through the cell cycle after MS, the more their gene expression programs were altered. Indeed, while only 150 deregulated genes were found in G1, 388 genes were deregulated in the subsequent G2 (Fig. 4G-H).

Overall, our results identified that MS perturbs 3D genome organisation and chromatin state in newly born tetraploid cells culminating with changes in gene expression programs.

Megakaryocytes undergo mitotic slippage and display nuclear instability

We decided to determine whether physiological polyploid cells generated by MS also exhibit nuclear deformations. To do so, we analysed megakaryocytes, differentiated polyploid cells, derived from hematopoietic progenitors[7], and responsible for production of RNAs and proteins that will be transported to the cell tips to generate anucleate platelets[10]. To obtain megakaryocytes, we isolated mouse diploid hematopoietic stem cells and induced their differentiation *in vitro* using a cocktail of cytokines (see methods and Fig. 5A). We obtained a population of primary cells composed of diploid hematopoietic stem cells and polyploid megakaryocytes showing different cell and nuclear sizes. These differences in size reflect a ploidy continuum and allow us to identify polyploid cells (Supp. Fig. 9A-B). Using live imaging approaches of megakaryocytes isolated from mice expressing H2B-mCherry, we observed that nuclei exit mitosis without chromosome segregation or following limited movement during anaphase A. These lack any sign of cytokinesis furrowing confirming MS (Figure 5B and Movie 10-11), as previously described[7,57].

In our hands, and in agreement with *in vivo* analysis[6,7], megakaryocytes displayed a single multilobulated highly deformed nucleus (Fig. 5C). Quantification of circularity and solidity revealed a decrease in a ploidy-dependent manner (Fig. 5D-E). Similarly to MS-induced RPE-1 cells, we observed that megakaryocyte nuclear shapes were highly heterogenous (Fig 5F). This reflects that megakaryocyte polyploidization by MS also generates nuclear instability. When comparing with other physiological polyploid cells, we noticed that nuclear instability was specific to megakaryocytes. Indeed, analysis of polyploid hepatocytes isolated from mouse liver, that become polyploid by cytokinesis failure (CF)[8,13] or *Drosophila* salivary glands, that become polyploid by endoreplication (EnR)[9,11], showed homogeneous circular nuclei lacking nuclear deformations (Fig. 5F and Supp. Fig. 9C-G). Similar observations were made *in vivo* in two other polyploid *Drosophila* tissues – the fat body and the ring gland that become polyploid by EnR (Supp. Fig. 9H)[3]. Importantly, quantifications of the nuclear circularity and solidity showed that these indices

remained stable during hepatocyte and salivary gland cell polyploidisation (Supp. Fig. 9I-L).

Together, these findings show that MS, but not CF or EnR impact nuclear shape and stability in physiological polyploid settings.

Phospho-methyl switch is responsible for nuclear deformations in megakaryocytes

Our results in RPE-1 cells show that MS-induced tetraploid cells fail to establish links between H3K9me2 chromatin and the Lamin A/C increasing nuclear deformability by the microtubule cytoskeleton. We therefore considered the possibility that megakaryocytes undergo a similar process. We first tested whether the microtubule cytoskeleton in megakaryocytes is associated with nuclear invaginations. Similarly to what we observed in RPE-1 cells, we found thick microtubule bundles positioned around nuclear invaginations (Fig. 6A), which were absent in hepatocytes or salivary glands. In these former examples, the microtubule cytoskeleton was organized around the nucleus forming a microtubule ring (Supp. Fig. 10A-B).

We then analysed H3K9me2 and Lamina composition. Although a decrease in H3K9me2 levels in deformed regions was evident in megakaryocytes, local changes in the lamina network were not detected (Fig. 6B-G). However, a striking switch in Lamina composition during megakaryocyte differentiation was observed. Small and large megakaryocytes displayed lower levels of Lamin A/C than hematopoietic stem cells, while Lamin B1 levels remained largely unchanged (Fig. 6B-G). Interestingly, this was associated with a transient increase in H3K27ac levels in small megakaryocytes (Supp. Fig. 10C-D). These findings suggest that during differentiation, megakaryocytes are in a state in which nuclear resistance is probably low favouring nuclear deformability by the microtubule cytoskeleton. In line with this, a previous study identified that nuclear stiffness decreased during megakaryocyte differentiation[58]. In contrast, defects in H3K9me2 distribution and Lamina composition in hepatocytes or in the Lamina network in salivary glands were not detected (Supp. Fig. 10E-O).

We next tested whether decreasing H3S10 phosphorylation in megakaryocytes could prevent nuclear deformations during their differentiation. To do so, we induced megakaryocyte differentiation in the presence of Methylstat or JIB,

two histone demethylase inhibitors[40,59], which resulted in increased H3K9 methylation levels and decreased H3S10 phosphorylation (Fig 6H-I and Supp. Fig. 10P). Strikingly, this was sufficient to alter nuclear shapes showed by a significant increased nuclear circularity and solidity in treated megakaryocytes (Fig 6J-K).

These results suggest that highly specialized and differentiated cells such as polyploid megakaryocytes rely on premature nuclear envelope reformation in conditions of high H3S10 phosphorylation to generates cells with irregular nuclear architecture *in vivo*. Importantly, our findings also identified the molecular mechanism underlying the irregular nuclear shape in megakaryocytes that was described 50 years ago[6].

Discussion

In this study, we identified that different means to induce WGD lead to different outcomes. Indeed, we showed that MS, unlike CF and EnR, generated tetraploid cells displaying abnormal nuclear configurations. These defects include (1) a local decrease in H3K9me2 and Lamin A/C levels that reduces nuclear stiffness facilitating the deformation of the tetraploid nuclei by the microtubule cytoskeleton. These findings are supported by other studies, which have shown that microtubules, Lamins and peripheral heterochromatin also dictate nuclear morphology in diploid cells[29,60–62]. The subsequent generation of nuclear invaginations upon MS produces a heterogenous population of polyploid nuclei with various shapes - (2) that we defined as nuclear instability - culminating with (3) changes in 3D genome organisation, chromatin state as well as in gene expression programs (Figure 6L). Importantly, we observed these defects in the first G1 upon MS contributing to a better understanding of the early consequences of WGD on nuclear architecture and 3D genome organization.

MS, CF and EnR have been proposed to be at the origin of WGD in tumours[2,13,24], but little is known about their proportion and respective role in cancer. Nuclear deformations were observed in tumours since the mid-nineteenth century and are even used for diagnostic in some situations[63], but a potential link with WGD and MS was never established. It remains to be understood whether nuclear deformations and instability, typical of MS, contribute to the tumorigenic process. MS, CF and EnR are also involved in developmental programs generating physiological polyploid cells[7–9,64]. Whether these different strategies reflect a particular advantage or are just byproducts of selective pressure remains unknown.

Interestingly, to our knowledge, megakaryocytes are the only example of MS-generated physiological polyploid cells, making them quite unique. By showing that megakaryocytes display defects in H3K9me2 levels at the nuclear envelope that contributes to nuclear deformations, we exposed a molecular mechanism underlying the generation of megakaryocytes with irregular nuclear architecture. It has been shown that megakaryocyte reprogramming to induce polyploidy through EnR instead of MS contributes to prevent nuclear deformations[57], confirming the predominant role of MS in generating megakaryocytes with irregular architecture. The global changes in chromatin state and distribution that we observed upon MS may contribute to

alterations in gene expression sustaining the required transcriptomic changes described during megakaryocyte differentiation[65].

Our observations may also contribute to a better comprehension of the role of nuclear deformations in diploid cells. Indeed, neutrophils, a different kind of hematopoietic cell that remain diploid during their differentiation[66], exhibit striking nuclear deformations associated with low levels of H3K9me2, HP1α and Lamin A/C[67,68].

Overall, our findings show that the cell cycle route chosen to generate polyploid cells has different outcomes. More importantly, our results highlight the fact that in physiological and pathological conditions, different methods to induce WGD have the potential to generate polyploid cells with specific features contributing to their inherent function.

Acknowledgments

The authors acknowledge the Cell and Tissue Imaging (PICT-IBiSA) from Institut Curie, member of the national infrastructure France-BioImaging (https://ror.org/01y7vt929) supported by the French National Research Agency (ANR-24-INBS-0005 FBI BIOGEN) and V. Fraisier, C. Guedj. M. David, M. Cortes and A.S. Macé (PICT-IBiSA) for their continuous support on image acquisition and analysis. We thank L. Guyonnet, A. Chipont, A.G. Lafont and C. Guerrin from the Cytometry platform of Institut Curie. High-throughput sequencing was performed by the ICGex NGS platform of the Institut Curie supported by the grants ANR-10-EQPX-03 (Equipex) and ANR-10-INBS-09-08 (France Génomique Consortium) from the Agence Nationale de la Recherche ("Investissements d'Avenir" program), by the ITMO-Cancer Aviesan (Plan Cancer III) and by the SiRIC-Curie program (SiRIC Grant INCa-DGOS-465 and INCa-DGOS-Inserm_12554). Data management, quality control and primary analysis were performed by the Bioinformatics platform of the Institut Curie. We thank Genosplice (http://www.genosplice.com) and more specifically P. Delagrange and M. Caron for RNAseq and ChIPseq analysis and for their valuable work. We thank A. Rodriguez-Romera and B. Psaila for sharing unpublished work. We thank A. Poleshko and JA Epstein for sharing the plasmids expressing H3WT and H3S10A. We thank A. Donada, J. Cossgrove and L. Perie, for teaching us the secrets of megakaryocyte differentiation and together with M. Piel and U. Kutay for helpful discussions and/or comments on the manuscript. GA's team has been supported by the European Research Council (ERC-2015-ADG-694694 ChromADICT), the Ligue Nationale contre le Cancer (Equipe labellisée Ligue), France and Agence Nationale de la Recherche, France (ANR-11-LABX-0044_DEEP, ANR-10-IDEX-0001-02 PSL). N.W has been supported by the FRM. This work has been funded by InCA (www.e-cancer.fr) (2021-1- PREV-Bio grant), the government through the Agence Nationale de la Recherche from France 2030 (ANR-23-CHBS-0012), the Institut Curie and the CNRS.

Author's contribution

S.G. and R.B. conceived the project. S.G. wrote the manuscript. S.G. and M.B. did most of the experiments and data analysis presented here. S.A., F.SdC., C.V. and V.M. contributed to the HSC purification. S.A. prepared the RNA used for the RNAseq. Y.M. and S.W. performed the AFM with the help of S.G. and M.B. J.F. and

C.D. contributed by isolating the mouse hepatocytes. R.L., G.C. and E.O. performed the HiC experiments. N.W, A.F. and G.A. designed and performed the ChIPseq experiments with the help of S.G. and M.B. R.B. obtained the funding used to develop this project. All authors read and commented on the manuscript.

Declaration of interests

The authors declare no competing interests.

References

1. Gemble, S. & Basto, R. CHRONOCRISIS: When Cell Cycle Asynchrony Generates DNA Damage in Polyploid Cells. *BioEssays News Rev. Mol. Cell. Dev. Biol.* **42**, e2000105 (2020).
2. Ganem, N. J., Storchova, Z. & Pellman, D. Tetraploidy, aneuploidy and cancer. *Curr. Opin. Genet. Dev.* **17**, 157–162 (2007).
3. Orr-Weaver, T. L. When bigger is better: the role of polyploidy in organogenesis. *Trends Genet.* **31**, 307–315 (2015).
4. Bielski, C. M. *et al.* Genome doubling shapes the evolution and prognosis of advanced cancers. *Nat. Genet.* **50**, 1189–1195 (2018).
5. Zack, T. I. *et al.* Pan-cancer patterns of somatic copy number alteration. *Nat. Genet.* **45**, 1134–1140 (2013).
6. Penington, D. G. & Streatfield, K. Heterogeneity of megakaryocytes and platelets. *Ser. Haematol. 1968* **8**, 22–48 (1975).
7. Mazzi, S., Lordier, L., Debili, N., Raslova, H. & Vainchenker, W. Megakaryocyte and polyploidization. *Exp. Hematol.* **57**, 1–13 (2018).
8. Gentric, G. & Desdouets, C. Liver polyploidy: Dr Jekyll or Mr Hide? *Oncotarget* **6**, 8430–8431 (2015).
9. Frawley, L. E. & Orr-Weaver, T. L. Polyploidy. *Curr. Biol. CB* **25**, R353-358 (2015).
10. Carminita, E., Becker, I. C. & Italiano, J. E. What It Takes To Be a Platelet: Evolving Concepts in Platelet Production. *Circ. Res.* **135**, 540–549 (2024).
11. Zielke, N. *et al.* Control of Drosophila endocycles by E2F and CRL4(CDT2). *Nature* **480**, 123–127 (2011).
12. Sigrist, S. J. & Lehner, C. F. Drosophila fizzy-related down-regulates mitotic cyclins and is required for cell proliferation arrest and entry into endocycles. *Cell* **90**, 671–681 (1997).
13. Davoli, T. & de Lange, T. The causes and consequences of polyploidy in normal development and cancer. *Annu. Rev. Cell Dev. Biol.* **27**, 585–610 (2011).
14. Nano, M. *et al.* Cell-Cycle Asynchrony Generates DNA Damage at Mitotic Entry in Polyploid Cells. *Curr. Biol.* **29**, 3937-3945.e7 (2019).
15. Gemble, S. *et al.* Genetic instability from a single S phase after whole-genome duplication. *Nature* **604**, 146–151 (2022).
16. Kirsch-Volders, M., Mišík, M. & Fenech, M. Tetraploidy in normal tissues and diseases: mechanisms and consequences. *Chromosoma* **134**, 3 (2025).
17. Goupil, A. *et al.* Chromosomes function as a barrier to mitotic spindle bipolarity in polyploid cells. *J. Cell Biol.* **219**, e201908006 (2020).
18. López, S. *et al.* Interplay between whole-genome doubling and the accumulation of deleterious alterations in cancer evolution. *Nat. Genet.* **52**, 283–293 (2020).
19. Prasad, K. *et al.* Whole-Genome Duplication Shapes the Aneuploidy Landscape of Human Cancers. *Cancer Res.* **82**, 1736–1752 (2022).
20. Kuznetsova, A. Y. *et al.* Chromosomal instability, tolerance of mitotic errors and multidrug resistance are promoted by tetraploidization in human cells. *Cell Cycle Georget. Tex* **14**, 2810–2820 (2015).
21. Blakely, C. M. *et al.* Evolution and clinical impact of co-occurring genetic alterations in advanced-stage EGFR-mutant lung cancers. *Nat. Genet.* **49**, 1693–1704 (2017).
22. Basu, S., Greenwood, J., Jones, A. W. & Nurse, P. Core control principles of the eukaryotic cell cycle. *Nature* **607**, 381–386 (2022).

23. Guidotti, J.-E. *et al.* Liver cell polyploidization: a pivotal role for binuclear hepatocytes. *J. Biol. Chem.* **278**, 19095–19101 (2003).
24. Zeng, J., Hills, S. A., Ozono, E. & Diffley, J. F. X. Cyclin E-induced replicative stress drives p53-dependent whole-genome duplication. *Cell* **186**, 528-542.e14 (2023).
25. Bernhard, S. V., Gemble, S., Basto, R. & Storchova, Z. Experimental Approaches to Generate and Isolate Human Tetraploid Cells. *Methods Mol. Biol. Clifton NJ* **2545**, 391–399 (2023).
26. Ganem, N. J. *et al.* Cytokinesis Failure Triggers Hippo Tumor Suppressor Pathway Activation. *Cell* **158**, 833–848 (2014).
27. Vittoria, M. A. *et al.* A genome-wide microRNA screen identifies regulators of tetraploid cell proliferation. *Mol. Biol. Cell* **29**, 1682–1692 (2018).
28. Kuffer, C., Kuznetsova, A. Y. & Storchová, Z. Abnormal mitosis triggers p53-dependent cell cycle arrest in human tetraploid cells. *Chromosoma* **122**, 305–318 (2013).
29. Stephens, A. D., Banigan, E. J. & Marko, J. F. Chromatin's physical properties shape the nucleus and its functions. *Curr. Opin. Cell Biol.* **58**, 76–84 (2019).
30. Miroshnikova, Y. A. & Wickström, S. A. Mechanical Forces in Nuclear Organization. *Cold Spring Harb. Perspect. Biol.* **14**, a039685 (2022).
31. Dechat, T., Adam, S. A., Taimen, P., Shimi, T. & Goldman, R. D. Nuclear lamins. *Cold Spring Harb. Perspect. Biol.* **2**, a000547 (2010).
32. Lammerding, J. *et al.* Lamins A and C but not lamin B1 regulate nuclear mechanics. *J. Biol. Chem.* **281**, 25768–25780 (2006).
33. Poleshko, A. *et al.* H3K9me2 orchestrates inheritance of spatial positioning of peripheral heterochromatin through mitosis. *eLife* **8**, e49278 (2019).
34. Janin, A., Bauer, D., Ratti, F., Millat, G. & Méjat, A. Nuclear envelopathies: a complex LINC between nuclear envelope and pathology. *Orphanet J. Rare Dis.* **12**, 147 (2017).
35. Delaney, K., Weiss, N. & Almouzni, G. The cell-cycle choreography of H3 variants shapes the genome. *Mol. Cell* **83**, 3773–3786 (2023).
36. Chen, Y.-J. C., Koutelou, E. & Dent, S. Y. R. Now open: Evolving insights to the roles of lysine acetylation in chromatin organization and function. *Mol. Cell* **82**, 716–727 (2022).
37. Maison, C. & Almouzni, G. HP1 and the dynamics of heterochromatin maintenance. *Nat. Rev. Mol. Cell Biol.* **5**, 296–304 (2004).
38. James, T. C. *et al.* Distribution patterns of HP1, a heterochromatin-associated nonhistone chromosomal protein of Drosophila. *Eur. J. Cell Biol.* **50**, 170–180 (1989).
39. Bowers, E. M. *et al.* Virtual ligand screening of the p300/CBP histone acetyltransferase: identification of a selective small molecule inhibitor. *Chem. Biol.* **17**, 471–482 (2010).
40. Stephens, A. D. *et al.* Chromatin histone modifications and rigidity affect nuclear morphology independent of lamins. *Mol. Biol. Cell* **29**, 220–233 (2018).
41. Moreno-Andrés, D., Holl, K. & Antonin, W. The second half of mitosis and its implications in cancer biology. *Semin. Cancer Biol.* **88**, 1–17 (2023).
42. Rothballer, A. & Kutay, U. The diverse functional LINCs of the nuclear envelope to the cytoskeleton and chromatin. *Chromosoma* **122**, 415–429 (2013).
43. De Brabander, M., De May, J., Joniau, M. & Geuens, G. Ultrastructural immunocytochemical distribution of tubulin in cultured cells treated with microtubule inhibitors. *Cell Biol. Int. Rep.* **1**, 177–183 (1977).

44. Manfredi, J. J. & Horwitz, S. B. Taxol: an antimitotic agent with a new mechanism of action. *Pharmacol. Ther.* **25**, 83–125 (1984).
45. Ovsiannikova, N. L. *et al.* Lamin A as a Determinant of Mechanical Properties of the Cell Nucleus in Health and Disease. *Biochem. Biokhimiia* **86**, 1288–1300 (2021).
46. Swift, J. *et al.* Nuclear lamin-A scales with tissue stiffness and enhances matrix-directed differentiation. *Science* **341**, 1240104 (2013).
47. Prigent, C. & Dimitrov, S. Phosphorylation of serine 10 in histone H3, what for? *J. Cell Sci.* **116**, 3677–3685 (2003).
48. Hendzel, M. J. *et al.* Mitosis-specific phosphorylation of histone H3 initiates primarily within pericentromeric heterochromatin during G2 and spreads in an ordered fashion coincident with mitotic chromosome condensation. *Chromosoma* **106**, 348–360 (1997).
49. Hsu, J. Y. *et al.* Mitotic phosphorylation of histone H3 is governed by Ipl1/aurora kinase and Glc7/PP1 phosphatase in budding yeast and nematodes. *Cell* **102**, 279–291 (2000).
50. Marxer, M., Ma, H. T., Man, W. Y. & Poon, R. Y. C. p53 deficiency enhances mitotic arrest and slippage induced by pharmacological inhibition of Aurora kinases. *Oncogene* **33**, 3550–3560 (2014).
51. Afonso, O., Figueiredo, A. C. & Maiato, H. Late mitotic functions of Aurora kinases. *Chromosoma* **126**, 93–103 (2017).
52. Wang, F. & Higgins, J. M. G. Histone modifications and mitosis: countermarks, landmarks, and bookmarks. *Trends Cell Biol.* **23**, 175–184 (2013).
53. Duan, Q., Chen, H., Costa, M. & Dai, W. Phosphorylation of H3S10 blocks the access of H3K9 by specific antibodies and histone methyltransferase. Implication in regulating chromatin dynamics and epigenetic inheritance during mitosis. *J. Biol. Chem.* **283**, 33585–33590 (2008).
54. Ishihara, H. *et al.* Calyculin A and okadaic acid: inhibitors of protein phosphatase activity. *Biochem. Biophys. Res. Commun.* **159**, 871–877 (1989).
55. Lambuta, R. A. *et al.* Whole-genome doubling drives oncogenic loss of chromatin segregation. *Nature* **615**, 925–933 (2023).
56. Padeken, J., Methot, S. P. & Gasser, S. M. Establishment of H3K9-methylated heterochromatin and its functions in tissue differentiation and maintenance. *Nat. Rev. Mol. Cell Biol.* **23**, 623–640 (2022).
57. Trakala, M. *et al.* Functional reprogramming of polyploidization in megakaryocytes. *Dev. Cell* **32**, 155–167 (2015).
58. Shin, J.-W. *et al.* Lamins regulate cell trafficking and lineage maturation of adult human hematopoietic cells. *Proc. Natl. Acad. Sci. U. S. A.* **110**, 18892–18897 (2013).
59. Wang, L. *et al.* A small molecule modulates Jumonji histone demethylase activity and selectively inhibits cancer growth. *Nat. Commun.* **4**, 2035 (2013).
60. Biedzinski, S. *et al.* Microtubules control nuclear shape and gene expression during early stages of hematopoietic differentiation. *EMBO J.* **39**, e103957 (2020).
61. Tariq, Z. *et al.* Lamin A and microtubules collaborate to maintain nuclear morphology. *Nucl. Austin Tex* **8**, 433–446 (2017).
62. Nava, M. M. *et al.* Heterochromatin-Driven Nuclear Softening Protects the Genome against Mechanical Stress-Induced Damage. *Cell* **181**, 800-817.e22 (2020).

63. de Las Heras, J. I. & Schirmer, E. C. The nuclear envelope and cancer: a diagnostic perspective and historical overview. *Adv. Exp. Med. Biol.* **773**, 5–26 (2014).
64. Girdler, G. C. & Röper, K. Controlling cell shape changes during salivary gland tube formation in Drosophila. *Semin. Cell Dev. Biol.* **31**, 74–81 (2014).
65. De Wispelaere, K. & Freson, K. The Analysis of the Human Megakaryocyte and Platelet Coding Transcriptome in Healthy and Diseased Subjects. *Int. J. Mol. Sci.* **23**, 7647 (2022).
66. Carvalho, L. O., Aquino, E. N., Neves, A. C. D. & Fontes, W. The Neutrophil Nucleus and Its Role in Neutrophilic Function. *J. Cell. Biochem.* **116**, 1831–1836 (2015).
67. Lukásová, E. *et al.* Methylation of histones in myeloid leukemias as a potential marker of granulocyte abnormalities. *J. Leukoc. Biol.* **77**, 100–111 (2005).
68. Olins, A. L. *et al.* The human granulocyte nucleus: Unusual nuclear envelope and heterochromatin composition. *Eur. J. Cell Biol.* **87**, 279–290 (2008).

METHODS

Human cell culture and generation of cell lines:

- *Cell culture:*

Cells were maintained at 37°C in a 5% CO_2 atmosphere. hTERT RPE-1 cells (female, ATCC Cat# CRL-4000, RRID:CVCL_4388), HEK293T cells (female, ATCC Cat# CRL-1573, RRID:CVCL_0045), BJ cells (male, ATCC Cat# CRL-4001, RRID:CVCL_6573) and HCT116 cells (male, ATCC Cat# CCL-247, RRID:CVCL_0291) were grown in Dulbecco's modified medium (DMEM) F12 (11320-033 from Gibco) containing 10% fetal bovine serum (GE Healthcare), 100 U/ml penicillin, 100 U/ml streptomycin (15140-122 from Gibco).

All cells were routinely checked and tested negative for mycoplasma infection. Identity and purity of the human cell lines used in this study were tested and confirmed using STR authentication.

- *Generation of RPE-1 GFP-H3 WT and GFP-H3S10A stable cell lines:*

RPE-1 cells were transfected with 10µg GFP-H3 WT and GFP-H3S10A[2] using JET PRIME kit (Polyplus Transfection, 114-07) according to the manufacturer's protocol. After 24hrs, 500µg/ml G418 (4727878001 from Roche) was added to the cell culture medium. After 72hrs of antibiotic selection GFP-positive cells were then collected using Sony SH800 FACS (BD FACSDiva Software Version 8.0.1).

GFP-H3 WT and GFP-H3S10A plasmids were a gift of Epstein JA[2].

- *Generation of RPE-1 GFP-Lamin and mCherry H2B stable cell line:*

RPE-1 mCherry cells[3] were transfected with 10µg GFP Lamin chromobodies (Icg from Chromotek) using JET PRIME kit (Polyplus Transfection, 114-07) according to the manufacturer's protocol. After 24hrs, 500µg/ml G418 was added to the cell culture medium. After 72hrs of antibiotic selection mCherry-H2B and GFP-positive (Lamin chromobodies) cells were then collected using Sony SH800 FACS (BD FACSDiva Software Version 8.0.1).

- *Generation of RPE-1 KASH-DN stable cell line:*

To produce lentiviral particles, HEK293T cells were transfected with 4µg pinducer 20 DN-KASH (12554 from Addgene, RRID:Addgene_125554) + 4µg pMD2.G (12259 from Addgene, RRID:Addgene_12259) + 4µg psPAX2 (12260 from Addgene, RRID:Addgene_12260) using a FuGENE HD Transfection Reagent (E2311 from Promega) in OptiMEM medium (51985034 from ThermoFisher). Cells were incubated at 37°C in a 5% CO2 atmosphere for 16hrs and then growth media were removed and replaced by 5 ml fresh

OptiMEM. The following day, viral particles were isolated by filtering the medium containing them through a 0.45µm filter (16537 from Sartorius stedim biotech). Then, RPE-1 cells were incubated with viral particles in the presence of 8µg/ml polybrene (sc-134220 from Santa Cruz) at 37°C in a 5% CO_2 atmosphere for 24hrs. Then, 500µg/ml G418 (4727878001 from Sigma Aldrich) was added to the cell culture medium. After 72hrs of antibiotic selection cells were collected.

pinducer 20 DN-KASH was a gift from Daniel Conway[4] - Addgene plasmid #125554; http://n2t.net/addgene:125554; RRID:Addgene_125554.

Transgenic Animals:

For animal care, we followed the European and French National Regulation for the Protection of Vertebrate Animals used for Experimental and other Scientific Purposes (Directive 2010/63; French Decree 2013-118). The project was authorized and benefited from guidance of the Animal Welfare Body, Research Centre, Curie Institute. All mice were kept in the Curie Institute Specific Pathogen Free (SPF) animal facility for breeding. The transgenic R26-H2B-mCherry mouse line[1] was back-crossed in our animal facility on a C57Bl6/N genetic background (Charles River, France). Only heterozygous R26-H2B-mCherry +/- and control littermate males between 3 and 6 months of age were included in the analysis. Animals were anaesthetized by inhalation of isoflurane (Baxter, DDG9621) before being sacrificed by cervical dislocation for bone tissue collection.

Mouse Megakaryocyte *in vitro* differentiation and cell culture:

- *Hematopoietic progenitor enrichment*

Tibias and femurs from 2 to 6-months old mice were dissected from the mouse and excess tissue was removed using scalpels. One epiphyse of each bone was cut ant the opened bone was placed into a 1.5mL centrifugation tube containing a 200uL tip. The bones were then centrifuged at high speed during 10 seconds in an Eppendorf tube to eject the bone marrow cells. The cells were resuspended in 1ml of cold RPMI containing 10% fetal bovine serum (GE Healthcare), 100 U/ml penicillin, 100 U/ml streptomycin (15140-122 from Gibco), Anti-Anti (11570486 from Gibco) - hereafter called complete RPMI medium - and centrifuged for 5min at 1700rpm, 4°C.

125µl of cold complete RPMI medium were used to resuspend the cells, then 25µl of anti-CD117 magnetic beads (130-097-146 from Miltenyi Biotec) were added and mix to the cells. Cells were incubated on ice for 30min with the beads. Then, 1ml of cold complete RPMI medium was added to the cells and they were filtered through a 100µm cell strainer (431752 from Coning) into 50ml tubes. The tubes and the cell strainers were washed with an additional 1ml of cold complete RPMI medium. Cells were centrifuged for 5min at 1700rpm,

4°C. During the centrifugation, a MS column (130-042-201 from Miltenyi Biotec) was prewet with 2ml of cold complete RPMI medium and installed on MACS magnet (130-042-501 from Miltenyi Biotec). The cells were then resuspended in 1ml of cold complete RPMI medium and transferred to a 2ml tube. Using an insulin syringe fitted with a short 25G needle (300400 from BD Bioscience), cells were transferred to the column. After, the tubes and the columns were washed using 2ml of cold complete RPMI medium. The CD117-positive fraction was then collected in a tube by pouring the cells using a plunger. The CD117-positive cells were centrifuge for 5min at 1700rpm, 4°C and resuspended in 500µl of cold complete RPMI medium.

- *Cell culture and In vitro differentiation:*

Purified CD117-positive cells were cultured on coverslips pre-treated with PolyLysine (0.02mg/ml during 5', 37°C; HY-126437B from MedChemExpress) and Fibronectin (20µL in 500µl PBS, ON 37°C; F1141-5MG from Sigma-Aldrich) in DMEM-F12 + 10% fetal bovine serum (GE Healthcare) + 100 U/ml penicillin, 100 U/ml streptomycin (15140-122 from Gibco). Cells were maintained at 37°C in a 5% CO_2 atmosphere. Megakaryocyte differentiation was induced by adding mSCF (50 ng/mL; 250-03 from Peprotech) + mTPO (50 ng/mL; 315-14 from Peprotech) for at least 3 days.

Isolation of mouse Hepatocytes:

Two old C57B6J mice were anesthetized with an intra-peritoneal injection of 10 mg/kg xylazine and 100 mg/kg ketamine. Primary hepatocytes were isolated by the two-step liver collagenase perfusion method and seeded in complete medium, as described previously[5]. Briefly, after caudal vena cava catheterization and portal vein opening, livers were washed with 50 mL of perfusion solution containing 10 mM 4-(2-hydroxyethyl)-1-piperazineethanesulfonic acid (HEPES, Merck #H6147), 137 mM NaCl (Merck #5886), 2.68 mM KCl (Merck #P5405), 232 µM Na2HPO4 (Merck #S5136), 0.5 mM ethylenediaminetetraacetic acid (EDTA, Thermo Fisher Scientific #15575020) dissolved in deionized sterile water. Then, livers were digested with a collagenase solution containing 0.5 mg/mL of collagenase type IV (from Clostridium histolyticum, Merck #C5138) diluted in perfusion solution, and 10 mM of CaCl2 (Merck #C7902). After isolation, hepatocytes were collected, washed, and resuspended in complete medium: William's E medium GlutaMAX (Thermo Fisher Scientific #32551020) supplemented with bovine serum albumin 0,1% (Merck #A8412), penicillin-streptomycin 100 U/mL (Thermo Fisher Scientific #15140122), fungizone B 100 µg/mL (Thermo Fisher Scientific #15290026), dexamethasone 25 nM (Merck #D2915) and supplemented with 10% decomplemented foetal bovine serum (FBS, Thermo Fisher Scientific #10270106). The cell viability was equivalent in all groups (≥ 85%)

as assessed by the Trypan blue exclusion method. Hepatocytes were seeded at a density of 6.0e+5 in 6-cm dishes and incubated at 37°C under an atmosphere containing 5% (v/v) CO2, for 4 hours, to allow the cells to adhere. The medium was then replaced with fresh FBS-free complete medium which remained unchanged for the 24h of primary culture.

Fly husbandry and fly stocks

Flies were raised on cornmeal medium (0.75% agar, 3.5% organic wheat flour, 5.0% yeast, 5.5% sugar, 2.5% nipagin, 1.0% penicillin-streptomycin and 0.4% propionic acid). Fly stocks were maintained at 18 °C. Stocks used in this study: w[1118] (3605 from Bloomington).

In all experiments, larvae were staged to obtain comparable stages of development. Egg collection was performed at 25 °C for 24 h. After development at 25 °C, third instar larvae were used for dissection.

Treatments:

- *Induction of WGD in human cell lines*

To induce mitotic slippage, cells were incubated with DMSO (D8418 from Sigma Aldrich) or with a combination of 50µM Monastrol (S8439 from Selleckchem) + 1µM MPI-0479605 (S7488 from Selleckchem) for at least 4hrs.

Alternatively, to induce mitotic slippage, CCNB1 depletion in RPE CCNB1^{AID} cells was induced as described before[6]. Briefly, cells were treated with 2µg/ml Doxycycline (D3447 from Sigma Aldrich) + 3µM Asunaprevir (S4935 from Selleckchem) for 2hrs. Then, 500 µM Auxin (I5148 from Sigma Aldrich) was added to the cell culture medium for at least 4hrs.

Mitotic slippage was induced using the combination of Monastrol + MPI-0479605 unless it is specified in the figure legends.

To induce cytokinesis failure, cells were incubated with DMSO (D8418 from Sigma Aldrich) or with 20µM Blebbistatin (B0560 from Sigma) or with 20µM Paprotrain (HY-101298 from Medchem) for at least 4hrs. Actin staining using Phaloidin (A30107 from ThermoFisher) was used to ascertain the binucleation of the CF-generated tetraploid cells.

Cytokinesis failure was induced using Blebbistatin unless it is specified in the figure legends.

To induce endoreplication, cells were incubated with DMSO (D8418 from Sigma Aldrich) or with 20µM SP600125 (HY-12041 from Medchem) for at least 4hrs.

Alternatively, to induce endoreplication, CCNA2 depletion in RPE CCNA2^{AID} cells was induced as described before[6]. Briefly, cells were treated with 2µg/ml Doxycycline (D3447 from Sigma Aldrich) + 3µM Asunaprevir (S4935 from Selleckchem) for 2hrs. Then, 500 µM Auxin (I5148 from Sigma Aldrich) was added to the cell culture medium for at least 4hrs.

Endoreplication was induced using SP600125 unless it is specified in the figure legends.

Each treatment generates a mixed population of diploid and tetraploid cells. After synchronizing cells in G1 (see the “Cell cycle synchronization” section), diploid (2N) and tetraploid (4N) cells are easily distinguished based on their nuclear size measured using Image J software V2.1.0/1.53c, https://imagej.net/software/fiji/downloads, as previously described[3].

- *Cell cycle synchronization*

To obtain a synchronous population of G1 cells, after 4hrs of WGD induction (see “Induction of WGD in human cell lines” section) 1µM Palbociclib (Cdk4/6 inhibitor, S1579 from Selleckchem) was added to the cell culture media for 16hrs to synchronize cells at the G1/S transition.

To analyze the first G2 upon WGD, Palbociclib was washed five times using PBS 1X and cells were released in the presence of 10µM RO-3306 (HY-12529 from Medchem) to block them in G2.

- *Strategies to increase H3K9me*

To promote H3K9me2, we used multiple complementary genetic and chemical approaches including inhibitors targeting histone demethylase (4µM Methylstat, 5µM JIB and 30µM, GSK-J4), transient PHF8 (a histone demethylase) depletion using siRNA or transient over-expression of G9a (a histone methylase). These strategies induced a significant increase in H3K9me levels assessed by immunofluorescence.

- *Chemicals*

Methylstat, JIB, GSK-J4, C646, Barasertib, Nocodazole and Taxol were added 2hrs before the induction of mitotic slippage.

Alternatively, cells were treated with Nocodazole or Methylstat for 2hrs after the mitotic slippage by washing the cell culture media five times with PBS 1X before to add the drugs.

Cells were treated with Calyculin A for 2:30hrs before fixation.

Megakaryocytes were incubated with Methylstat and JIB for 6hrs three days after the addition of the cytokines. To analyze megakaryocytes that performed mitotic slippage in the presence of the drugs only the small megakaryocytes were taken into account.

To extend mitotic duration, cells were treated with 50µM Monastrol for 16hrs and then 1µM MPI-0479605 was added for 2hrs to induce the mitotic slippage before fixing the cells.

The drugs were used at the following concentrations: Auxin (I5148 from Sigma), 500µM; Doxycycline (D3447 from Sigma), 2µg/ml; Asunaprevir (S4935 from Selleckchem), 3µM; Monastrol (S8439 from Selleckchem), 50µM; MPI-0479605 (S7488 from Selleckchem), 1µM; Blebbistatin (B0560 from Sigma), 20µM; Palbociclib (S1579 from Selleckchem), 1µM; Methylstat (HY-15221 from Medchem), 2 or 4µM; GSK-J4 (HY-15648B from Medchem), 30µM, JIB (HY-13953 from MedChemExpress), 2,5 or 5µM, Nocodazole (HY-13520 from Medchem), 2µM; Taxol (T1912 from Sigma), 1nM; SP600125 (HY-12041 from Medchem), 20µM; RO3306 (HY-12529 from Medchem), 10µM; Calyculin A (HY-18983 from Medchem), 5nM; Barasertib (HY-10127 from Medchem), 0.1 and 1µM; C646 (HY-13823 from Medchem), 30µM.

- *Transfection*

PHF8 depletion: RPE-1 cells on coverslips were transfected using 50nM of siRNA specific for PHF8 (L-004291-01-000524225 from Dharmacon) with a JET PRIME kit (Polyplus Transfection, 114-07) according to the manufacturer's protocol. 48hrs later, the coverslips were transferred to new wells and incubated with DMSO (D8418 from Sigma Aldrich) or with 50µM Monastrol (S8439 from Selleckchem) + 1µM MPI-0479605 (S7488 from Selleckchem) to generate tetraploid cells. After 2hrs, 1µM Palbociclib (S1579 from Sellechem) was added to the cell culture medium for 16hrs. Cells were then fixed in G1 and analyzed. In parallel, cells that were not on the coverslips were used to prepare whole cell extract (see the "*Western Blot"* section) to confirm siRNA efficiency.
A pool of 4 different siRNA was used: CUCAUGAGUGCAGAUA; UCAAGAAGGCAGAGCAAA; GGUGAUGGAAGACGAAUUU and UGGGAGUGUUAGUAAUCAA.

G9a over expression: RPE-1 cells on coverslips were transfected using 2µg of pCMV-HA-hG9a (Addgene 33024; RRID:Addgene_33024) with a JET PRIME kit (Polyplus Transfection, 114-07) according to the manufacturer's protocol. 24hrs later, the coverslips were transferred to new wells and incubated with DMSO (D8418 from Sigma Aldrich) or with 50µM Monastrol (S8439 from Selleckchem) + 1µM MPI-0479605 (S7488 from Selleckchem) to generate tetraploid cells. After 2hrs, 1µM Palbociclib (S1579 from Sellechem) was added to the cell culture medium for 16hrs. Cells were then fixed in G1 and analyzed. In parallel, cells that were not on the coverslips were used to prepare whole cell extract (see the "*Western Blot"* section) to confirm G9a overexpression.

Immunofluorescence:

- *Preparation and imaging of human cells*

Cells were plated on cover slips in 12-well plates and treated with the indicated drugs. To label cells, they were fixed using 4% of paraformaldehyde (15710 from Electron Microscopy Sciences) + Triton X-100 (2000-C from Euromedex) 0,1% in PBS (20 min at 4°C). Then, cells were washed three times using PBS-T (PBS 1X + 0,1% Triton X-100 + 0,02% Sodium Azide) and incubated with PBS-T + BSA (04-100-812-C from Euromedex) 1% for 30 min at RT. After three washes with PBS-T + BSA, primary and secondary antibodies were incubated in PBS-T + BSA 1% for 1hr and 30 min at RT, respectively. After two washes with PBS, cells were incubated with 3 µg/ml DAPI (4',6-diamidino-2-phenylindole; D8417 from Sigma Aldrich) for 15 min at RT. After two washes with PBS, slides were mounted using 1.25% n-propyl gallate (Sigma, P3130), 75% glycerol (bidistilled, 99.5%, VWR, 24388-295), 23.75% H2O.

Images were acquired on an upright widefield microscope (DM6B, Leica Systems, Germany) equipped with a motorized XY and a 40X objective (HCX PL APO 40X/1,40-0,70 Oil from Leica). Acquisitions were performed using Metamorph 7.10.1 software (Molecular Devices, USA) and a sCMOS camera (Flash 4V2, Hamamatsu, Japan). Stacks of conventional fluorescence images were collected automatically at a Z-distance of 0.5 µm (Metamorph 7.10.1 software; Molecular Devices, RRID:SCR_002368).

For H3.1/2 and H3.3 staining, two additional extractions were done, a pre-extraction (Triton X-100, 0,1%, 30sec) before the fixation and a post-extraction (Triton X-100, 0,5%, 5min) after the fixation.

- *Preparation and imaging of mouse megakaryocytes and mouse hepatocytes*

For megakaryocytes, cells were plated on cover slips in 24-well plates and fixed using 4% of paraformaldehyde (15710 from Electron Microscopy Sciences) + Triton X-100 (2000-C from Euromedex) 0,1% in PBS (20 min at 4°C) or for microtubule staining with 100% cold MetOH (32213 from Honeywell). For hepatocytes, cells were plated on cover slips in 6-well plates and fixed using 4% of paraformaldehyde (15710 from Electron Microscopy Sciences) or for microtubule staining with 100% MetOH (32213 from Honeywell).

Then, cells were washed three times using PBS-T (PBS 1X + 0,1% Triton X-100 + 0,02% Sodium Azide) and incubated with PBS-T + 1% BSA (04-100-812-C from Euromedex) 1% for 30 min at RT. After three washes with PBS-T + BSA, primary and secondary antibodies were incubated in PBS-T + BSA 1% for 3hrs and 2hrs at RT, respectively. After two washes with PBS, cells were incubated with 3 µg/ml DAPI (4',6-diamidino-2-phenylindole; D8417 from Sigma Aldrich) for 15 min at RT. After two washes with PBS, slides were mounted using 1.25% n-propyl gallate (Sigma, P3130), 75% glycerol (bidistilled, 99.5%, VWR, 24388-295), 23.75% H2O.

Images were acquired on a spinning disk microscope (Gataca Systems, France). Based on a CSU-W1 (Yokogawa, Japan), the spinning head was mounted on an inverted Eclipse Ti2 microscope equipped with a motorized XY Stage (Nikon, Japan). Images were acquired through a 100x 1.4NA Plan-Apo objective with a sCMOS camera (Prime95B, Photometrics, USA). Optical sectioning was achieved using a piezo stage (Nano-z series, Mad City Lab, USA). Gataca Systems' laser bench was equipped with 405, 491 and 561 nm laser diodes, delivering 150 mW each, coupled to the spinning disk head through a single mode fibre. Multi-dimensional acquisitions were performed using Metamorph 7.10.1 software (Molecular Devices, USA).

- *Preparation and imaging of Drosophila salivary glands*

Drosophila salivary glands from third instar larvae were dissected in PBS and fixed for 30 min in 4% paraformaldehyde in PBS. They were washed 3 times in PBST 0.3% (PBS, 0.3% Triton X-100, T9284 from Sigma), 15 min for each wash, and incubated for 1 hr with blocking solution (PBS, 0.3% Triton X-100 + 5% normal goat serum, 10098792 from Gibco). Then salivary glands were washed 3 times in PBS, 15 min for each wash and incubated overnight at 4 °C with primary antibodies at the appropriate dilution in the blocking solution. Tissues were washed three times in PBST 0.3%, 15 min for each wash, and incubated overnight at 4 °C with secondary antibodies diluted in the blocking solution. Salivary glands were then washed 3 times in PBST 0.3%, 15 min for each wash, rinsed in PBS and incubated with 3 µg ml−1 DAPI (4′,6-diamidino-2-phenylindole; Sigma Aldrich D8417) at room temperature for 30 min. Salivary glands were then washed in PBS at room temperature for 30 min and mounted in clearing solution (Rapiclear 1.49 Sunjin Lab, RC149002).

Images were acquired as previously described in the section "*Preparation and imaging of mouse megakaryocytes and mouse hepatocytes"*.

- *Super-resolution microscopy:*

Images were acquired as previously described in the section "*Preparation and imaging of mouse megakaryocytes and mouse hepatocytes"*.

Super resolution was achieved on the CSU-W1 spinning disk equipped with a super-resolution module (Live-SR, Gataca systems). This module is based on structured illumination with optical reassignment technique and online processing leading to a two-time resolution improvement. The method called multifocal SIM (MSIM) allows combining the doubling resolution together with the physical optical sectioning of confocal microscopy.

- *Primary and secondary antibodies*

Primary and secondary antibodies were used at the following concentrations: β-catenin (1/250; C2206 from Sigma-Aldrich, RRID:AB_476831), Lamin A/C (1/500; SAB4200236 from Sigma Aldrich, RRID:AB_10743057), Lamin B1 (1/500; ab16048 from Abcam, RRID:AB_443298), H3S10 (1/500, ab14955 from Abcam, RRID:AB_443110), Lamin A/C (1:50, ADL101 from DHSB, RRID:AB_528332), Lamin B (1/50, ADL67.10 from DHSB, RRID:AB_528336), H3K9ac (1/500, 9649S from Ozyme; RRID:AB_823528), H3K27ac (1/500, 39685 from Active Motif, RRID:AB_2793305), DM1A (1/1000, T9026 from Sigma Aldrich, RRID:AB_477593), H3K9me2 (1/500, 39239 from Active Motif, RRID:AB_2793199), H3K9me3 (1/500, ab8898 from Abcam, RRID:AB_306848), H3K27me3 (1/500, 39155 from Active motif, RRID:AB_2561020), HP1 (1/500, ab109028 from Abcam, RRID:AB_10858495), H4K20me2 (1/500, 720085 from ThermoFisher, RRID:AB_2532798), H3.1/2 (1/500, 61629 from Active Motif, RRID:AB_2793710), H3K27ac (1/500, 39685 from Active Motif, RRID:AB_2793305), H3.3 (1/500, 91191 from Active Motif, RRID:AB_279379), Lap2β (1/250, 611000 from BD Bioscience, RRID:AB_398313), LBR (1/500, ab232731 from Abcam, RRID:AB_3246426), Nuclear Pore Complex (1/250, ab24609 from Abcam, RRID:AB_448181), Emerin (1/150, 10351-1-AP from ProteinTech, RRID:AB_2100056), Sun1 (1/200, HPA008346 from Atlas Antibodies, RRID:AB_1080462), Sun2 (1/200, HPA001209 from Atlas Antibodies, RRID:AB_1080465), Nesprin 1 (1/100, MANNES1E from Wolfson Centre for Inherited Neuromuscular Disease, RRID:AB_2753303), Nesprin 2 (1/100, MANNES2A(11A3) from Wolfson Centre for Inherited Neuromuscular Disease, RRID:AB_2753305), goat anti-Rabbit IgG (H+L) Highly Cross-Adsorbed Secondary Antibody, Alexa Fluor 647 (1/250; A21245 from ThermoFisher, RRID:AB_2535813), Goat anti-Rabbit IgG (H+L) Highly Cross-Adsorbed Secondary Antibody, Alexa Fluor 546 (1/250; A-11035 from ThermoFisher, RRID:AB_2534093), Goat anti-Mouse IgG1 Cross-Adsorbed Secondary Antibody, Alexa Fluor™ 488 (1/250, A-21121 from ThermoFisher, RRID:AB_2535764), Goat anti-Mouse IgG2b Cross-Adsorbed Secondary Antibody, Alexa Fluor™ 488 (1/250, A-21141 from ThermoFisher, RRID:AB_2535778), Goat anti-Mouse IgG2a Cross-Adsorbed Secondary Antibody, Alexa Fluor™ 546 (1/250, A-21133 from ThermoFisher, RRID:AB_2535772), Alexa Fluor™ Plus 647 Phalloidin (1/2000, A30107 from ThermoFisher).

3D cultures:

- *Mitotic slippage on 3D cultures*

To generate spheroids, 500 cells per well were seeded into 96 ultra-low attachment well plates (7007 from Corning) in presence of DMSO (D8418 from Sigma Aldrich) or with 50µM monastrol (S8439 from Selleckchem) and 1µM MPI-0479605 (S7488 from Selleckchem).

Plates were spun down at 200g for 3min, to allow spheroid formation, and incubated for 24hrs at 37°C.

- *Immunostaining*

Spheroids were collected and washed quickly with PBS prior fixation using 4% of paraformaldehyde (15710 from Electron Microscopy Sciences) in PBS for 40min. Then, spheroids were permeabilized for 5 min using Triton X-100 (2000-C from Euromedex) 0,3% in PBS and blocked for 30min using Blocking Buffer (BB= PBS 1X + 0,3% Triton X-100 + 0,02% Sodium Azide + 3% BSA). Aggregates were incubated with primary antibodies diluted into BB O/N. After 3 washes using BB, spheroids were incubated with secondary antibodies in BB for 3hrs. Cells were then washed several times for 2hrs in BB and mounted on glass with EverBrite (Biotium). For primary and secondary antibodies see *Immunofluorescence microscopy and antibodies* section.

Time lapse microscopy:

Cells were plated on a dish (627870 from Greiner). Methylstat (2µM) or Nocodazole (2µM) were added two hours before to start the movies. To follow microtubules or actin, SPY650-Tubulin (SC503 from Tebubio) or SPY650-FastAct (SC505 from Tebubio), respectively, were added one hour before to start the movie.

Images were acquired on a spinning disk microscope (Gataca Systems, France). Based on a CSU-W1 (Yokogawa, Japan), the spinning head was mounted on an inverted Eclipse Ti2 microscope equipped with a motorized XY Stage (Nikon, Japan). Images were acquired through a 40X NA 1.3 oil objective with a sCMOS camera (Prime95B, Photometrics, USA). Optical sectioning was achieved using a piezo stage (Nano-z series, Mad City Lab, USA). Gataca Systems' laser bench was equipped with 405, 491 and 561 nm laser diodes, delivering 150 mW each, coupled to the spinning disk head through a single mode fiber. Laser power was chosen to obtain the best ratio of signal/background while avoiding phototoxicity. Multi-dimensional acquisitions were performed using Metamorph 7.10.1 software (Molecular Devices, USA). Stacks of conventional fluorescence images were collected automatically at a Z-distance of 0.5 µm (Metamorph 7.10.1 software; Molecular Devices, RRID:SCR_002368). Images are presented as maximum intensity projections generated with ImageJ software (RRID:SCR_002285), from stacks deconvolved with an extension of Metamorph 7.10.1 software.

Western Blot:

For a whole-cell extract, cells were lysed in 8 M urea, 50 mM Tris HCl, pH 7.5 and 150 mM β-mercaptoethanol (161-0710 from Bio-Rad), sonicated and heated at 95°C for 10 minutes.

Then, samples (equivalent of 2 x 10^5 cells) were subjected to electrophoresis in NuPAGE Novex 4–12% Bis-Tris pre-cast gels (NP0321 from Life Technologies). The same number of cells were loaded. Protein fractions from the gel were electrophoretically transferred to PVDF membranes (PVDF transfer membrane; RPN303F from GE). After 1hr saturation in PBS containing 5% dry non-fat milk and 0.5% Tween 20, the membranes were incubated for 1hr with a primary antibody (*see below*) diluted in PBS containing 5% dry non-fat milk and 0.5% Tween 20. After three 10-min washes with PBS containing 0.5% Tween 20, the membranes were incubated for 45 min with a 1/2 500 dilution of peroxidase-conjugated antibody (*see below*). Membranes were then washed three times with PBS containing 0.5% Tween 20, and the reaction was developed according to the manufacturer's specifications using ECL reagent (SuperSignal West Pico Chemiluminescent Substrate; 34080 from Thermo Scientific).

- *Primary and secondary antibodies*

Primary and secondary antibodies were used at the following concentrations GAPDH (1/500, 2118 from Cell Signaling, RRID:AB_561053), PHF8 (1/500, 39711 from Active Motif, RRID:AB_2793316), HA (sc-7392 from Santa Cruz Biotechnology, RRID:AB_627809); Goat anti-Rabbit IgG (H+L) Cross-Adsorbed Secondary Antibody, HRP (1/2500; G21234 from ThermoFisher, RRID:AB_2536530), Peroxidase AffiniPure Goat Anti-Mouse IgG (H+L) (1/2500; 115-035-003 from Jackson ImmunoResearch, RRID:AB_10015289).

FACS of diploid and tetraploid cells:

A mix of diploid and tetraploid cells synchronized in G1 or in G2/M (see “Cell cycle synchronization” section) were incubated with 2 µg ml−1 Hoescht 33342 (Sigma Aldrich 94403) for 1 h at 37 °C, 5% CO2. Then, a single cell suspension was generated. Cells were washed using PBS, the supernatant was removed, and cells were resuspended in cell culture medium containing 1µM EDTA (10135423 from Invitrogen). Fluorescence-activated cell sorting (FACS) was performed using Sony SH800 FACS (BD FACSDiva Software Version 8.0.1), as previously described[3]. Compensations were performed using the appropriate negative control samples.

HiC experiment:

Diploid and tetraploid cells were isolated using flow cytometry (see “FACS of diploid and tetraploid cells” section). Diploid and tetraploid cells were isolated using flow cytometry (see “FACS of diploid and tetraploid cells” section). Library preparation for Hi-C was conducted as previously described[7]. Briefly, the cells were fixed with formaldehyde, and fixed nuclei were extracted for further processing. Chromatin was digested with MboI restriction enzyme (New

England Biolabs, R0147), and digested ends were biotinylated. Next, a proximity ligation was carried out, followed by chromatin crosslink reversal. DNA was purified, sheared via sonication, and size-selected for library preparation. Biotin-marked DNA fragments were pulled down with Dynabeads MyOne Streptavidin C1 (Thermo Fisher Scientific, 65001). Hi-C library preparation continued with end polishing, A-tailing, and Illumina TruSeq unique dual indexes ligation reactions. Lastly, libraries were amplified via PCR, and sequenced on an Illumina HiSeq X platform, PE150 configuration.

Atomic force microscopy:

Atomic Force Microscopy measurements were performed on glass bottom dishes (ibidi) with a JPK NanoWizard 4 (Bruker Nano) microscope mounted on an Eclipse Ti2 inverted fluorescent microscope (Nikon) and operated via JPK SPM Control Software v.6. MLCT triangular silicon nitride cantilevers (Bruker) were used to access the mechanical properties of nuclei. Forces of up to 2 nN were applied at 10 micron per second constant cantilever velocity also ensuring an indentation depth of at ~500 nm.

Native Chromatin Immunoprecipitation:

- *Sample preparation*

We isolated Diploid and tetraploid G1 cells using flow cytometry (see “FACS of diploid and tetraploid cells” section) and used 2.5 x10^6 cells per condition. We performed native nucleosome isolation as previously described[8] at 4°C in the presence of protease inhibitors with the following modifications. We used 2.5 x10^6 FACS-sorted cells per IP, processed by Mnase digestion (37C, 10min). After inhibition with 20mM EGTA and centrifugation (10,000g, 10min), we processed sample pellets in 100 uL lysis buffer (50 mM Tris HCl pH 7.5, 150 mM NaCl, 5 mM CaCl2, 1% Triton X-100, 0.5% NP40) by sonication (Bioruptor Pico, Diagenode, High 5 cycles, 30s on, 30s off). After another centrifugation (10,000g, 10min) we combined like-supernatants from each step for each sample and carried out Bradford assay (Pierce Bradford assay kit, 23200, ThermoFisher). We performed Histone PTM ChIP-seq as previously described[9,10] with the following modifications including addition of spike-in controls (61686 and 53083 from Active motif) in accordance with manufacturer’s instructions. Briefly, each IP reaction used 75 uL of Ab-conjugated beads after 4 hours incubation in Bead blocking buffer (2.5% BSA in PBS-T, 1 mg/mL tRNA), washing once in 0.02% PBS-T and coupling with the antibodies (diluted in 0.2mL 0.02% PBS-T) on a rotating wheel for 30 min, 4°C. We washed Ab-conjugated beads twice with 0.02% PBS-T and resuspended in 0.2 mL 0.02% PBS-T. We diluted the prepared native nucleosomes (~115 µg per IP) in 4x volumes of Incubation buffer (50 mM Tris-HCl pH 7.5, 100 mM NaCl, 0.5% BSA) and pre-cleared with unconjugated Dynabeads Protein A (15 µL per input pool) (1002D, Invitrogen) for 30 min on

a rotating wheel. Sample were incubated with Ab-conjugated beads (washed once in Incubation buffer) overnight (4°C on a rotating wheel) and DNA purified as described for SNAP-seq in Gatto et al.[8].

We used Qubit dsDNA HS Assay kit for DNA quantification (Q32851 from ThermoFisher) and TapeStation & High Sensitivity D1000 ScreenTape with HS D1000 (5067-5584 from Agilent) to obtain the MNase profile in order to validate and control sample quality before High-Throughput Sequencing.

- *Sequencing*

We prepared libraries from input and immunoprecipitated DNAs using the KAPA Hyper Prep Kit (KK8504 from ROCHE) according to manufacturer's protocol. Briefly, 2 to 6 ng of DNA were subjected to subsequent steps of end-repair, dA-tailing and ligation of Illumina barcoded adapters. After a final PCR amplification step (14 cycles), individual library quantification and quality assessment was performed using Qubit fluorometric assay (Invitrogen) with dsDNA HS (High Sensitivity) Assay Kit and LabChip GX Touch using a High Sensitivity DNA chip (Perkin Elmer). Libraries were then equimolarly pooled and quantified by qPCR using the KAPA library quantification kit (Roche). Sequencing was carried out on the NovaSeq X Plus instrument from Illumina using paired-end 2 x 100 bp, to obtain around 50 million clusters (100 million raw paired-end reads) per sample.

Total RNAseq:

- *RNA preparation*

Diploid and tetraploid G1 or G2/M cells were isolated using flow cytometry (see "FACS of diploid and tetraploid cells" section). Then RNA was extracted using All Prep DNA/RNA Mini Kit (80204 from Qiagen) according to the manufacturer's protocol. To normalize, RNA Spike-in were added to the samples (4456740 from Invitrogen) according to the manufacturer's protocol. 1 x 10^6 cells were used per condition (3n).

To control the quality of the samples before High-Throughput Sequencing, RNAs were analyzed to quantify the RIN using Agilent RNA 6000 Nano Kit (5067-1511 from Agilent).

- *Sequencing*

We prepared RNA sequencing libraries from 500ng of total RNA using the Illumina® Stranded Total RNA Prep and the Ligation with Ribo-Zero Plus library preparation kit, which allows to perform a strand specific sequencing. This protocol includes a first step of enzymatic depletion of abundant transcripts from multiple species using specific probes. We then perfomed cDNA synthesis and used resulting fragments for dA-tailing followed by ligation of RNA Index Anchors. PCR amplification with indexed primers (IDT for Illumina RNA

UD Indexes) was finally achieved, with 13 cycles, to generate the final cDNA libraries. Individual library quantification and quality assessment was performed using Qubit fluorometric assay (Invitrogen) with dsDNA HS (High Sensitivity) Assay Kit and LabChip GX Touch using a High Sensitivity DNA chip (Perkin Elmer). Libraries were then equimolarly pooled and quantified by qPCR using the KAPA library quantification kit (Roche). Sequencing was carried out on the NovaSeq X Plus instrument from Illumina using paired-end 2 x 100 bp, to obtain around 100 million clusters (200 million raw paired-end reads) per sample.

QUANTIFICATION AND STATISTICAL ANALYSIS

Immunofluorescence:

Image analysis and quantifications were performed using Image J software V2.1.0/1.53c, https://imagej.net/software/fiji/downloads[11]. Images are presented as maximum intensity projections generated with ImageJ software (RRID:SCR_002285).

For the 3D reconstruction, images were converted in Imaris files using ImarisFileConverter 9.9.1 (Bitplane, RRID:SCR_007370). Then, images were imported into Imaris software v.9.6.0 (Bitplane, RRID:SCR_007370). Nuclear shapes were reconstructed based on the DNA staining. 3D views were generated using Imaris software and saved as TIFF.

To quantitatively measure nuclear shapes, the “wand” tool from Image J V2.1.0/1.53c software was used to select the nuclei based on the DAPI staining and then the circularity and solidity indexes were measured using the “shape descriptors” tool from Image J V2.1.0/1.53c software.

For the mini screen, images were converted into maximum intensity projections and the mean fluorescence intensity at the whole nucleus was measured using the “polygon sections” tool from Image J V2.1.0/1.53c software while the mean fluorescence intensity at the nuclear envelope or locally at the intact/deformed regions were measured using the “segmented lines” tool from Image J V2.1.0/1.53c software. Since diploid cells were not deformed, the mean fluorescence intensity was compared at two random regions to visualize the distribution of the signal, while in newly born tetraploid cells, intact and deformed areas were compared.

The coefficient of variation (CoV) was measured by dividing the standard deviation of the signal by the mean fluorescence intensity for each cell.

To define small and large megakaryocytes or hepatocytes, the median nuclear size was used as a threshold.

For the figures, images were processed on Image J V2.1.0/1.53c software, and mounted using Affinity Designer 2, https://affinity.serif.com/fr/designer/.

Time lapse microscopy:

Image analysis and quantifications were performed using Image J software V2.1.0/1.53c, https://imagej.net/software/fiji/downloads. Videos were corrected using “3D correct drift” plugin with Image J V2.1.0/1.53c software to keep the cell of interest at the center of the region of interest.

For the Figure 2D, nuclei masks were generated using the Fiji Plugin as described in[12]. Briefly, this process involves denoising (using the Pure Denoise Fiji Plugin[13]) and thresholding the image over time, to get one ROI (the nucleus) on each frame. A custom

macro was then used to project the contours over time, with each contour colored according to its corresponding frame. The Analyze Particles function was applied to the masks generated by the Plugin, and the contours' ROIs were color-coded according to their frame using BAR Plugin.

To analyze nuclear shapes by live imaging, single cells were followed, and nuclear circularity and solidity indexes were measured in G2 before the NEBD and in G1 after complete DNA decondensation. The results were plotted using the “before-after” representation from GraphPad Prism (RRID:SCR_002798) version 10 for Mac, GraphPad Software, La Jolla California USA, www.graphpad.com. The delta circularity was measured by dividing the nuclear circularity index in G2 by the one in G1 for each single cell.

For the figures, images were processed on Image J V2.1.0/1.53c software, and mounted using Affinity Designer 2, https://affinity.serif.com/fr/designer/.

Western blot:

The images were acquired using an iBright1500 from Invitrogen and analyzed using Image Lab software version 6.0.1, Bio-Rad Laboratories. The background-adjusted volume intensity was calculated and normalized using a GAPDH signal for each protein.

For the figures, images were processed using Image Lab software version 6.0.1, Bio-Rad Laboratories, and mounted using Affinity Designer 2, https://affinity.serif.com/fr/designer/.

Total RNAseq data:

Analysis of sequencing data quality, reads repartition (e.g., for potential ribosomal contamination), inner distance size estimation, genebody coverage, strand-specificity of library were performed using FastQC, Picard-Tools, Samtools, and RSeQC. Reads were mapped using STAR on the Human hg38 genome assembly and read count was performed using featureCount from SubRead and the Human FAST DB v2022_1 annotations.

Gene expression was estimated as described previously[14]. Only genes expressed in at least one of the two compared conditions were analyzed further. Genes were considered as expressed if their FPKM value was greater than FPKM of 98% of the intergenic regions (background). Analysis at the gene level was performed using DESeq2[15]. Genes were considered differentially expressed for fold-changes ≥ 1.5 and p-values ≤ 0.05.

Overrepresented analyses and GSEA[16] were performed using WebGestalt[17] merging results from up-regulated and down-regulated genes only, as well as all regulated genes. Pathways and networks were considered significant with p-values ≤ 0.05.

VolcanoPlots were created using ggplot2. In blue are genes that are differentially under-expressed in the Tetraploid condition, and in red those that are over-expressed (based on thresholds indicated after the use of DESeq2).

Native Chromatin Immunoprecipitation data:

Quality control was performed using FastQC, ChIPQC and MultiQC. Sequencing reads were aligned to the human reference genome (hg38) using the BWA-MEM algorithm. Duplicate reads were marked using the Picard MarkDuplicates tool. Only reads with a mapping quality score ≥40 were retained, using Samtools. Spike-in normalization was conducted following the guidelines provided by ActiveMotif. Briefly, the number of reads uniquely mapped to the Drosophila (dm6) genome was quantified per sample. A normalization ratio was then calculated based on the lowest number of Drosophila-mapped reads among all samples. This ratio was subsequently applied to downsample the uniquely mapped reads to the human genome in each sample with Samtools. Peak calling was performed with MACS3 callpeak (--BAMPE), using an Input sample as control. Differential peak analysis was carried out using the bdgdiff module from MACS3. Finally, peak annotation was performed using HOMER.

ManhattanPlots are generated with ggplot2. Each bar represents enriched peaks (from bdgdiff analysis) count which is normalized by chromosome arm or cytoband length respectively. Finally, values are multiplied by 10 million.

Karyoplots were generated using karyoploteR. The genome is sliced into 0.5e6bp windows and each peak represents a density of enriched peaks (from bdgdiff analysis).

Atomic force microscopy:

Analyses were performed with JPK Data Processing Software v.6 (Bruker Nano) by 1) removing the offset from the baseline of raw force curves, 2) identifying the contact point and subtracting cantilever bending then 3) fitting the Hertz model with correct tip geometry to quantitate the reported Young's Modulus of nuclei.

HiC data:

For Hi-C data, reads were mapped to the human hg19 reference genome. Generation of Hi-C contact maps and further analyses, including inter-chromosomal interactions, intercompartmental interactions, and conservation of insulating boundaries were performed as previously described[7].

Statistical analysis:

The statistical significance of differences was calculated using GraphPad Prism (RRID:SCR_002798) version 10 for Mac, GraphPad Software, La Jolla California USA, www.graphpad.com. The statistical test used for each experiment is indicated in the figure legends. Each representative image originates from the analyzed dataset and are

representative of the associated quantifications. ns=not significant. *=P ≤ 0.05. **= P ≤ 0.01. ***= P ≤ 0.001. ****= P ≤ 0.0001.

REFERENCES METHOD SECTION

1. Abe, T. *et al.* Establishment of conditional reporter mouse lines at ROSA26 locus for live cell imaging. *Genes. N. Y. N 2000* **49**, 579–590 (2011).
2. Poleshko, A. *et al.* H3K9me2 orchestrates inheritance of spatial positioning of peripheral heterochromatin through mitosis. *eLife* **8**, e49278 (2019).
3. Gemble, S. *et al.* Genetic instability from a single S phase after whole-genome duplication. *Nature* **604**, 146–151 (2022).
4. Mayer, C. R., Arsenovic, P. T., Bathula, K., Denis, K. B. & Conway, D. E. Characterization of 3D Printed Stretching Devices for Imaging Force Transmission in Live-Cells. *Cell. Mol. Bioeng.* **12**, 289–300 (2019).
5. Donne, R. *et al.* Replication stress triggered by nucleotide pool imbalance drives DNA damage and cGAS-STING pathway activation in NAFLD. *Dev. Cell* **57**, 1728-1741.e6 (2022).
6. Hégarat, N. *et al.* Cyclin A triggers Mitosis either via the Greatwall kinase pathway or Cyclin B. *EMBO J.* **39**, e104419 (2020).
7. Lambuta, R. A. *et al.* Whole-genome doubling drives oncogenic loss of chromatin segregation. *Nature* **615**, 925–933 (2023).
8. Gatto, A., Forest, A., Quivy, J.-P. & Almouzni, G. HIRA-dependent boundaries between H3 variants shape early replication in mammals. *Mol. Cell* **82**, 1909-1923.e5 (2022).
9. Karagyozova, T. *et al.* HIRA-dependent provision of histone H3.3 in active chromatin ensures genome compartmentalisation. 2024.08.27.609896 Preprint at https://doi.org/10.1101/2024.08.27.609896 (2024).
10. Karagyozova, T. *et al.* HIRA defines early replication initiation zones independently of their genome compartment. 2024.08.29.610220 Preprint at https://doi.org/10.1101/2024.08.29.610220 (2024).
11. Schindelin, J. *et al.* Fiji: an open-source platform for biological-image analysis. *Nat. Methods* **9**, 676–682 (2012).
12. Almonacid, M. *et al.* Active Fluctuations of the Nuclear Envelope Shape the Transcriptional Dynamics in Oocytes. *Dev. Cell* **51**, 145-157.e10 (2019).
13. Luisier, F., Blu, T. & Unser, M. Image denoising in mixed Poisson-Gaussian noise. *IEEE Trans. Image Process. Publ. IEEE Signal Process. Soc.* **20**, 696–708 (2011).
14. Paillet, J. *et al.* Autoimmunity affecting the biliary tract fuels the immunosurveillance of cholangiocarcinoma. *J. Exp. Med.* **218**, e20200853 (2021).
15. Love, M. I., Huber, W. & Anders, S. Moderated estimation of fold change and dispersion for RNA-seq data with DESeq2. *Genome Biol.* **15**, 550 (2014).
16. Subramanian, A. *et al.* Gene set enrichment analysis: a knowledge-based approach for interpreting genome-wide expression profiles. *Proc. Natl. Acad. Sci. U. S. A.* **102**, 15545–15550 (2005).
17. Liao, Y., Wang, J., Jaehnig, E. J., Shi, Z. & Zhang, B. WebGestalt 2019: gene set analysis toolkit with revamped UIs and APIs. *Nucleic Acids Res.* **47**, W199–W205 (2019).

FIGURE LEGENDS

Figure 1: Unscheduled WGD induced through MS generates cells with nuclear instability

(A) Schematic representations of mitotic division (left panel) and of the different means employed to generate tetraploid cells (right panel). **(B)** Representative super resolution images and their corresponding 3D reconstructions showing nuclear shape in RPE-1 G1 cells upon canonical mitotic division, MS, CF and EnR. Lamin A/C in yellow, DNA in magenta. **(C-E)** Graphs showing the nuclear circularity and solidity index in G1 cells upon **(C)** MS (in blue), **(D)** CF (in yellow) and **(E)** EnR (in red). Mean ± SEM, >150 G1 cells analysed per condition, three independent experiments. **(F)** Stills of time lapse videos of RPE-1 cells stably expressing mCherry-H2B (in magenta) performing mitotic division (upper panel) or MS (lower panel). **(G-H)** Graph presenting the nuclear **(G)** circularity and **(H)** solidity measured at the single cell level in the same cells in G2 and in G1 upon mitotic division (in grey) or MS (in blue). >80 cells analysed per condition, three independent experiments. **(I)** Graph showing the delta circularity (defined as the difference between nuclear circularity in G2 vs in G1) upon mitotic division (in grey) or MS (in blue). Mean ± SEM, >75 cells analysed per condition, three independent experiments. **(J)** Representative images showing RPE-1 G1 nuclei upon mitotic division, MS, CF and EnR (upper panel). DNA in magenta. The nuclear contour is indicated (black dotted line, lower panel). Scale bars: 10µm. D=diploid; T=tetraploid; MS=mitotic slippage; CF=cytokinesis failure; EnR= endoreplication. NEBD=nuclear envelope breakdown. **(C,D,E)** ANOVA test (one-sided). **(G,H,I)** t-test (two-sided). ns=not significant. *=P ≤ 0.05. **= P ≤ 0.01. ***= P ≤ 0.001. ****= P ≤ 0.0001.

Figure 2: Mitotic slippage impairs the interaction between chromatin and the nuclear envelope

(A) Schematic representation showing the principle of atomic force microscopy (AFM). **(B)** Representative images showing diploid and MS-generated tetraploid G1 cells. DNA in magenta. Brightfield in grey. **(C)** Graph showing nuclear stiffness in diploid (in grey) and in MS-generated tetraploid G1 cells (in blue). Box and whiskers ± Min to Max, >90 cells analysed per condition, three independent experiments. **(D)** Left panel – Schematic workflow showing the methods used to measure fluorescence intensity in diploid and tetraploid cells. Fluorescence intensity was measured at two random regions in diploid cells and at intact and deformed regions in tetraploid cells. Right panel – Super resolution representative images of diploid and tetraploid G1 cells. Lamin A/C and H3K9me2 in yellow hot and cyan hot, respectively, DNA in magenta. **(E-F)** Graph showing **(E)** the relative H3K9me2 mean intensity and **(F)** the H3K9me2 coefficient of variation (defined as the ratio of the standard deviation to the mean) in diploid (in grey) and in MS-generated tetraploid G1 cells (in blue). Mean ± SEM, >90 G1 cells analysed per condition, three independent experiments. **(G-I)** Graph showing the relative **(G)** Lamin B1 and **(H)** Lamin A/C mean intensity at the NE and the **(I)** Lamin B1 vs Lamin A/C ratio at the NE in diploid (in grey) and in MS-generated tetraploid G1 cells (in blue). Mean ± SEM, >90 G1 cells analysed, three independent experiments. **(J)** Super resolution representative images of MS-generated tetraploid cells. Lamin A/C and Lamin B1 antibodies in yellow hot and red hot, respectively, DNA in magenta. **(K)** Working model showing nuclear deformations in newly born tetraploid cells generated by MS. Scale bars: 10µm. D=diploid; T=tetraploid; MS=mitotic slippage. EnR= endoreplication. NE= nuclear envelope. **(C)** Kolmogorov-Smirnov test. (**E,F,G,H,I**) t-test (two-sided). ns=not significant. *=P ≤ 0.05. **= P ≤ 0.01. ***= P ≤ 0.001. ****= P ≤ 0.0001.

Figure 3: Mitotic slippage allows mitotic exit with high H3 phosphorylation levels conditioning nuclear morphology

(A) Super resolution representative images showing mitotic diploid RPE-1 cells. H3S10 in green, DNA in magenta. **(B)** Graph showing H3S10 mean intensity during mitosis in diploid cells. Mean±SEM, >25 mitotic cells analysed per condition, three independent experiments. **(C-D)** Graph showing the nuclear **(C)** circularity and **(D)** solidity in diploid (in grey) and MS-generated tetraploid (in blue) RPE-1 G1 cells stably expressing H3WT or H3S10A. Mean±SEM, >150 cells analysed per condition, three independent experiments. **(E)** Super resolution representative images showing diploid and MS-generated tetraploid RPE-1 G1 cells stably expressing H3WT or H3S10A. Lamin A/C and H3K9me2 in yellow hot and cyan hot, respectively, DNA in magenta. **(F)** Schematic workflow showing the methods used to treat cells with Methylstat. **(G)** Super resolution representative images of diploid RPE-1 cells in prometaphase. H3K9me2 and H3S10 in cyan hot and green, respectively, DNA in magenta. **(H-I)** Graph showing the **(H)** H3S10 and **(I)** H3K9me2 mean intensity in early mitosis in RPE-1 diploid cells treated with DMSO or 4µM Methylstat. Mean±SEM, >100 mitotic cells analysed per condition, three independent experiments. **(J)** Super resolution representative images of RPE-1 G1 tetraploid cells treated with DMSO or 4µM Methylstat. H3K9me2 and Lamin A/C in cyan hot and yellow hot, respectively, DNA in magenta. **(K-L)** Graph showing nuclear **(K)** circularity and **(L)** solidity in diploid and in MS-generated tetraploid G1 cells treated with DMSO or 4µM Methylstat. Mean±SEM, >150 G1 cells analysed, three independent experiments. **(M-N)** Graph showing **(M)** the H3K9me2 coefficient of variation (define as the ratio of the standard deviation to the mean) and **(N)** the Lamin B1 vs Lamin A/C ratio at the NE in diploid and in MS-generated tetraploid G1 cells treated with DMSO or 4µM Methylstat. Mean±SEM, >85 G1 cells analysed per condition, three independent experiments. Scale bar: 10µm. D=diploid; T=tetraploid; MS=mitotic slippage. NE= nuclear envelope. (**B,C,D,K,L**) ANOVA test (one-sided). (**H,I,M,N**) t-test (two-sided). ns=not significant. *=P ≤ 0.05. **= P ≤ 0.01. ***= P ≤ 0.001. ****= P ≤ 0.0001.

Figure 4: Mitotic slippage impairs genome organisation and compaction and gene expression programs

(A) Schematic workflow showing the method used to isolate diploid and tetraploid G1 cells using flow cytometry. **(B)** Heatmap of the ratios of interchromosomal contact enrichments (observed versus expected) between RPE1 tetraploid (MS) and diploid cells. Chromosomes were sorted by length. **(C-D)** Graph showing the local enrichment of **(C)** H3K9me3 and **(D)** H3K9me2 at specific genomic regions. **(E)** Karyoplot of H3K9me3-enriched peaks density in the tetraploid (blue) and diploid (gray) condition on chromosome 2. The red arrows indicate regions that are enriched for H3K9me3 in both diploid and tetraploid conditions. **(F)** Karyoplot of H3K9me2-enriched peaks density in the tetraploid (blue) and diploid (gray) condition on chromosome 4. The red arrows indicate regions that are enriched for H3K9me2 only in diploid conditions. Green arrows indicate regions that are enriched for H3K9me2 only in tetraploid condition. **(G-H)** Volcanoplots of expressed genes in **(G)** G1 or **(H)** G2 cells. Diploid vs tetraploid ratio. Red points are over-expressed genes, and blue points are under-expressed genes (fold-changes ≥ 1.5 and p-values ≤ 0.05). MS=mitotic slippage. ns=not significant. *=P ≤ 0.05. **= P ≤ 0.01. ***= P ≤ 0.001. ****= P ≤ 0.0001.

Figure 5: Megakaryocytes undergo mitotic slippage and display nuclear instability

(A) Left panel - schematic workflow showing the methods used to induce megakaryocyte (MK) differentiation *in vitro*. Right panel – representative image showing Hematopoietic stem cells (HSC) and megakaryocytes. Actin in grey, DNA in magenta. **(B)** Stills of time lapse video showing MKs stably expressing mCherry-H2B (in magenta). Brightfield in grey. **(C)** Super resolution representative images and corresponding 3D reconstructions showing diploid HSC and polyploid megakaryocyte. Lamin A/C in yellow, DNA in magenta. **(D-E)** Graphs showing nuclear **(D)** circularity and **(E)** solidity in HSCs (in grey) and in megakaryocytes (in blue). Mean ± SEM, >65 interphase cells analysed per condition, three independent experiments. **(F)** Representative images of megakaryocyte, hepatocyte or salivary gland nuclei, the nuclear contour is indicated below. Scale bars: 10µm. HSC=Hematopoietic stem cells; MK=megakaryocytes. NEBD=nuclear envelope breakdown. **(D,E)** ANOVA test (one-sided). ns=not significant. *=P ≤ 0.05. **= P ≤ 0.01. ***= P ≤ 0.001. ****= P ≤ 0.0001.

Figure 6: Phospho-methyl switch is responsible for nuclear deformations in megakaryocytes

(A) Representative images of microtubules (in cyan) in megakaryocytes, DNA in magenta. **(B)** Super resolution representative images of HSC and megakaryocyte. H3K9me2 in cyan hot, DNA in magenta. **(C-D)** Graph showing H3K9me2 **(C)** mean intensity and **(D)** coefficient of variation (define as the ratio of the standard deviation to the mean) in HSCs (in grey) and in MKs (in blue). Mean±SEM, >150 interphase cells analysed per condition, four independent experiments. **(E)** Super resolution representative images showing HSC and megakaryocytes. Lamin A/C and Lamin B1 in yellow hot and red hot, respectively, DNA in magenta. **(F-G)** Graph showing **(F)** Lamin A/C and **(G)** Lamin B1 mean intensity at the NE in HSCs and in MKs. Mean±SEM, >35 cells analysed per condition, three independent experiments. **(H)** Representative images showing MKs in prometaphase treated with DMSO or 2µM Methylstat. H3S10 in green, DNA in magenta. **(I)** Graph showing H3S10 mean intensity in early mitosis in megakaryocytes treated with DMSO or 2µM Methylstat. Mean±SEM, >55 mitotic cells analysed per condition, three independent experiments. **(J)** Representative images showing MKs treated with DMSO or Methylstat. H3K9me2 in cyan hot, DNA in magenta. **(K)** Graph showing nuclear circularity (left panel) and solidity (right panel) in HSCs and in megakaryocytes treated with DMSO, 2µM Methylstat or 2,5µM JIB. Mean±SEM, >120 G1 cells analysed per condition, three independent experiments. **(L)** Working model showing the consequences of MS on nuclear stiffness and nuclear organisation. Upon MS, but not CF or EnR, nuclear instability at the population level can be identified. This has immediate consequences in chromatin organization, such as increasing the interactions between large and small chromosomes, leading to differential gene expression detected in a single cell cycle. Scale bars: 10µm. HSC=hematopoietic stem cell; MK=megakaryocyte; NE=nuclear envelope. (**C,D,I**) t-test (two-sided). (**F,G,K**) ANOVA test (one-sided). ns=not significant. *=P ≤ 0.05. **= P ≤ 0.01. ***= P ≤ 0.001. ****= P ≤ 0.0001.

Figure S1: Mitotic slippage unlike cytokinesis failure or endoreplication, generates polyploid cells with abnormal nuclear architecture

(A) Schematic representation showing the methods used to induce whole genome duplication. **(B)** Left panel – representative images showing diploid and CF-generated tetraploid RPE-1 G1 cells. β-Catenin in grey, DNA in magenta. Right panel – Graph showing nuclear circularity and solidity in diploid and in CF-generated tetraploid RPE-1 G1 cells (in grey and yellow, respectively). Mean±SEM, >100 G1 cells analysed per condition, three independent experiments. **(C-D)** Graphs showing nuclear circularity and solidity in diploid and in **(C)** MS- and **(D)** EnR-generated tetraploid RPE-1 G1 cells (in blue and red, respectively). Mean±SEM, >150 G1 cells analysed per condition, three independent experiments. **(E)** Graph presenting nuclear circularity and solidity in diploid and in MS-generated tetraploid HCT116 cells in G1 (in grey and blue, respectively). Mean±SEM, >100 G1 cells analysed per condition, three independent experiments. **(F)** Representative images showing diploid and MS-generated tetraploid HCT116 nuclei. DNA in magenta. **(G)** Graph showing nuclear circularity and solidity in diploid and in MS-generated tetraploid BJ cells in G1 (in grey and blue, respectively). Mean±SEM, >100 G1 cells analysed per condition, three independent experiments. **(H)** Representative images presenting diploid and MS-generated tetraploid BJ nuclei. DNA in magenta. **(I)** Graph showing nuclear circularity and solidity in diploid and in MS-generated tetraploid RPE-1 cells cultured in 3D (in grey and blue, respectively). Mean±SEM, >100 G1 cells analysed per condition, three independent experiments. **(J)** Representative images showing an RPE-1 spheroid containing diploid and MS-generated tetraploid cells. Actin in grey, DNA in magenta. **(K-L)** Graphs showing nuclear circularity and solidity in diploid and in MS-generated tetraploid **(K)** HCT116 and **(L)** BJ cells cultured in 3D (in grey and blue, respectively). Mean±SEM, >110 G1 cells analysed per condition, three independent experiments. **(M**) Graph showing nuclear circularity and solidity in diploid and in MS-generated tetraploid asynchronous RPE-1 cells (in grey and blue, respectively). Mean±SEM, >110 cells analysed per condition, three independent experiments. **(N-O)** Graphs presenting nuclear area in diploid and in MS- and EnR-generated tetraploid **(N)** RPE-1 and **(O)** HCT116 G1 cells (in grey, blue and red, respectively). Mean±SEM, >150 G1 cells analysed per condition, three independent experiments. **(P)** Graph showing nuclear circularity and solidity in diploid and in MS-generated tetraploid RPE-1 G2 cells (in grey and blue, respectively). Mean±SEM, >170 G2 cells analysed per condition, three independent experiments. **(Q)** Representative images showing diploid and MS-generated tetraploid RPE-1 shP53 cells. DNA in magenta. **(R-S)** Graph showing nuclear **(R)** circularity and **(S)** solidity in diploid and in MS-generated tetraploid RPE-1 shp53 cells (in grey and blue, respectively). Mean±SEM, >100 interphase cells analysed per condition, three independent experiments. Scale bars: 10µm. D=diploid; T=tetraploid; MS=mitotic slippage; CF=cytokinesis failure; EnR= endoreplication. (**B,C,D,E,G,M,N,O,P,R,S**) Anova-test (one sided). (**I,K,L**) t-test (two-sided). ns=not significant. *=P ≤ 0.05. **= P ≤ 0.01. ***= P ≤ 0.001. ****= P ≤ 0.0001.

1552

Figure S2: Visual screen of chromatin and nuclear envelope components in diploid and newly born tetraploid cells

(A) Schematic representation of the nucleus and of the surrounding cytoplasm. **(B)** Schematic workflow showing the methods used to perform the visual mini screen. Mean fluorescence intensity was measured in the whole nucleus, at the nuclear envelope or locally at two random regions (in diploid cells) and at intact and deformed regions (in tetraploid cells). **(C-E)** Graphs showing the mean fluorescence intensity measured at the whole nucleus (first line), at the nuclear envelope (second line) and at two different regions (third line) in diploid and in MS-generated tetraploid **(C-D)** RPE-1 cells or **(E)** RPE-1 CCNB1 cells (in grey and blue, respectively), as indicated. Mean ± SEM, >90 G1 cells analysed per condition, at least three independent experiments. **(F)** Super resolution representative images showing diploid and MS-generated tetraploid cells. H3K9ac (left panel) and H3K27ac (right panel) in cyan hot, DNA in magenta. **(G)** Left panel - super resolution representative images showing diploid and MS-generated tetraploid cells. HP1α in cyan hot, DNA in magenta. Right panel – Graph presenting the number of HP1α foci / nuclear area in diploid and in MS-generated tetraploid RPE-1 cells (in grey and blue, respectively). Mean ± SEM, >90 G1 cells analysed per condition, at least three independent experiments. Scale bars: 10µm. D=diploid; T=tetraploid. (**C,D,E,G**) t-test (two-sided). ns=not significant. *=P ≤ 0.05. **= P ≤ 0.01. ***= P ≤ 0.001. ****= P ≤ 0.0001.

Figure S3: Microtubules but not actin contributes to nuclear deformations in MS-induced newly born tetraploid cells

(A) Graph showing nuclear stiffness in diploid and in MS-generated tetraploid RPE-1 CCNB1 cells (in grey and blue, respectively). Box and whiskers□±□Min to Max, >175 G1 cells analysed per condition, three independent experiments. **(B)** Graph presenting H3K9ac mean intensity in RPE-1 diploid G1 cells treated with DMSO or with 30µM C646. Mean□±□SEM, >150 G1 cells analysed per condition, three independent experiments. **(C)** Super resolution representative images showing RPE-1 G1 cells treated with DMSO or with 30µM C646. H3K9ac in cyan hot, DNA in magenta. **(D)** Graph representing the nuclear area in diploid cells treated with DMSO or with 30µM C646. Mean□±□SEM, >110 G1 cells analysed per condition, three independent experiments **(E)** Graph showing nuclear circularity and solidity in diploid and in MS-generated tetraploid cells (in grey and cyan hot, respectively) treated with DMSO or with 30µM C646. Mean□±□SEM, >130 G1 cells analysed per condition, three independent experiments. **(F)** Stills of time lapse videos of RPE-1 cells stably expressing mCherry-H2B after mitotic division (upper panel) or MS (lower panel). The nuclear contour during G1 is indicated, and the colour code shows the time spent in G1 (see methods). The pink arrow indicates nuclear deformations. **(G)** Left panel - Graph showing the nuclear circularity and solidity in G1 upon mitotic division (in grey, upper panel) or MS (in blue, lower panel). The data were measured in cells presented in **(F)**. Right panel - Schematic representations of nuclear decondensation upon mitotic division (in grey, upper panel) or MS (in blue, lower panel). **(H)** Representative images of diploid and MS-generated tetraploid RPE-1 G1 cells. Microtubules in cyan, DNA in magenta. The nuclear contour is indicated (yellow dotted line). **(I)** Graph showing scan line measurements. Microtubule and DNA fluorescence intensities were measured at the nuclear deformations in the tetraploid cell presented in **(H)**. **(J)** Representative images showing diploid and MS-generated RPE-1 cells. Actin in grey, DNA in magenta. **(K)** Graph presenting scan line measurements. Actin and DNA fluorescence intensities were measured at the nuclear deformations in the tetraploid cell shown in **(J)**. **(L)** Representative images showing microtubules (in cyan) in diploid and in EnR-generated RPE-1 cells. DNA in magenta. **(M)** Stills of time lapse videos of RPE-1 cells stably expressing mCherry-H2B (in magenta undergoing MS. Microtubules in cyan. Scale bars: 10µm. D=diploid; T=tetraploid; MS=mitotic slippage. NEBD=nuclear envelope breakdown. AFM=Atomic force microscopy. **(L)** t-test (two-sided). (**A**) Kolmogorov-Smirnov test. (**B,D**) t-test (two-sided). (**E**) Anova-test (one-sided). ns=not significant. *=P ≤ 0.05. **= P ≤ 0.01. ***= P ≤ 0.001. ****= P ≤ 0.0001.

Figure S4: Microtubules but not actin contributes to nuclear deformations in MS-induced newly born tetraploid cells

(A) Stills of a time lapse movie showing RPE-1 cells stably expressing mCherry-H2B (in magenta) performing MS. Actin was labelled using SPY650-FastAct (in grey). **(B)** Representative images showing diploid RPE-1 cells stably expressing dox-inducible KASH DN treated with DMSO or with Dox for 8hrs. Nesprin 1 in green was used to show the efficiency of KASH-DN induction, DNA in magenta. **(C)** Graph showing nuclear circularity and solidity in diploid and in MS-generated tetraploid RPE-1 cells (in grey and blue, respectively) stably expressing dox-inducible KASH DN treated with DMSO or with Dox for 8hrs. Mean±SEM, >130 G1 cells analysed per condition, three independent experiments. **(D)** Stills of time lapse videos of RPE-1 cells stably expressing mCherry-H2B (in magenta) undergoing MS and treated with DMSO (upper panel) or nocodazole (lower panel). Microtubules in cyan. **(E)** Graph presenting the delta circularity (defined as the difference between nuclear circularity in G2 vs in G1) in MS-generated tetraploid cells treated with DMSO or 2µM Nocodazole. Mean±SEM, >90 cells analysed per condition, three independent experiments. **(F)** Schematic workflow showing the method used to treat the cells with Nocodazole. **(G)** Representative images showing the microtubule cytoskeleton in diploid and in MS-generated tetraploid RPE-1 cells treated with DMSO or with 2µM Nocodazole before or after MS. Microtubules in cyan, DNA in magenta. **(H)** Graph showing nuclear circularity and solidity in diploid and in MS-generated tetraploid RPE-1 cells (in grey and blue, respectively) treated with DMSO or with 2µM Nocodazole before or after MS. Mean±SEM, >105 G1 cells analysed per condition, three independent experiments. **(I)** Graph showing nuclear circularity and solidity in diploid and in MS-generated tetraploid RPE-1 CCNB1 cells (in grey and blue, respectively) treated with DMSO or with 2µM Nocodazole. Mean±SEM, >80 G1 cells analysed per condition, three independent experiments. **(J)** Stills of a time lapse movie showing RPE-1 CCNB1 cells stably expressing mCherry-H2B (in magenta) treated with DMSO or 2µM Nocodazole and performing MS. Microtubules were labelled using SPY650-Tubulin (in cyan). **(K)** Graph showing the delta circularity (defined as the difference between nuclear circularity in G2 vs in G1) upon mitotic division (in grey) or MS (in blue) treated with DMSO (-) or 2µM Nocodazole. Mean±SEM, >50 cells analysed per condition, three independent experiments. **(L)** Graph showing nuclear circularity and solidity in diploid and in MS-generated tetraploid RPE-1 cells (in grey and blue, respectively) treated with DMSO or with 1nM Taxol. Mean±SEM, >140 G1 cells analysed per condition, three independent experiments. Scale bars: 10µm. D=diploid; T=tetraploid; MS=mitotic slippage; CF=cytokinesis failure; EnR= endoreplication. (**E**) t-test (two-sided). (**C,H,I,K,L**) Anova-test (one-sided). ns=not significant. *=P ≤ 0.05. **= P ≤ 0.01. ***= P ≤ 0.001. ****= P ≤ 0.0001.

Figure S5: MS, but not CF and EnR, perturbs H3K9me2 and Lamin A/C distribution in tetraploid cells

(A) Graph showing the mean fluorescence intensity measured at the whole nucleus (first line) and at the nuclear envelope (second line) in diploid and in MS-generated tetraploid RPE-1 G1 cells (in grey and blue, respectively). Mean±SEM, >90 G1 cells analysed per condition, three or four independent experiments. **(B)** Super resolution representative images showing diploid and newly born tetraploid G1 cells. H3K9me3 in cyan hot, DNA in magenta. **(C)** Super resolution representative images of MS-generated tetraploid RPE-1 CCNB1 cells. Lamin A/C and Lamin B1 in yellow hot and red hot, respectively, DNA in magenta. **(D)** Graph showing (left panel) H3K9me2 coefficient of variation (defined as the ratio of the standard deviation to the mean) at the NE and (right panel) Lamin B1 vs Lamin A/C ratio at the NE in diploid (in grey) and in MS-generated tetraploid RPE-1 CCNB1 cells (in blue). Mean±SEM, >40 G1 cells analysed per condition, three independent experiments. **(E-F)** Graphs of H3K9me2 mean intensity at the NE (left panel), H3K9me2 coefficient of variation at the NE (central panel) and Lamin A/C mean intensity at the NE (right panel) in diploid and in MS-generated tetraploid (E) BJ and (F) HCT116 cells. Mean±SEM, >60 G1 cells analysed per condition, three independent experiments. **(G)** Super resolution representative images of MS-generated tetraploid BJ (left panel) and HCT116 (right panel) cells. Lamin A/C and H3K9me2 in yellow hot and cyan hot, respectively, DNA in magenta. **(H-I)** Super resolution representative images of **(H)** MS- and **(I)** EnR-generated tetraploid RPE-1 cells. Lamin A/C, Lamin B1 and H3K9me2 in yellow hot, red hot and cyan hot, respectively, DNA in magenta. **(J-K)** Graphs showing H3K9me2 mean intensity at the NE (left panel), H3K9me2 coefficient of variation at the NE (central panel) and Lamin B1 vs Lamin A/C ratio at the NE (right panel) in diploid and **(J)** CF- and **(K)** EnR-generated tetraploid RPE-1 cells (in grey, yellow and red, respectively). Mean±SEM, >90 G1 cells analysed per condition, three independent experiments. Scale bars: 10µm. D=diploid; T=tetraploid; MS=mitotic slippage; CF=cytokinesis failure; EnR= endoreplication; NE= nuclear envelope. (**A,D,C,F,J,K**) t-test (two-sided). ns=not significant. *=P ≤ 0.05. **= P ≤ 0.01. ***= P ≤ 0.001. ****= P ≤ 0.0001.

Figure S6: Promoting H3K9 methylation prevents nuclear deformations upon MS

(A) Representative images showing RPE-1 cells treated with DMSO or 1µM Barasertib. DNA in magenta. **(B)** Graph presenting nuclear circularity and solidity in RPE-1 cells treated with DMSO or 1µM Barasertib. Mean±SEM, >80 G1 cells analysed per condition, three independent experiments. **(C-D)** Graphs showing **(C)** H3S10 and **(D)** H3K9me2 mean intensity in early mitosis in RPE-1 cells stably expressing H3WT or H3S10. Mean±SEM, >60 mitotic cells analysed per condition, three independent experiments. **(E-F)** Graphs showing **(E)** H3K9me2 coefficient of variation (define as the ratio of the standard deviation to the mean) and **(F)** the Lamin B1 vs Lamin A/C ratio at the NE in diploid and in MS-generated tetraploid RPE-1 cells (in grey and blue, respectively) stably expressing H3WT or H3S10A. Mean±SEM, >80 G1 cells analysed, three independent experiments. **(G-H)** Graphs showing **(G)** H3K9me2 and **(H)** H3K9me3 mean intensity in RPE-1 interphase cells. Mean±SEM, >100 interphase cells analysed per condition, three independent experiments. **(I)** Stills of a time lapse movie showing RPE-1 cells stably expressing mCherry-H2B (in magenta) performing MS and treated with DMSO (upper panel) or 2µM Methylstat (lower panel). **(J-K)** Graphs showing the nuclear **(J)** circularity and **(K)** solidity measured at the single cell levels in G2 and in G1 upon mitotic division (in grey) or MS (in blue) in RPE-1 cells treated with DMSO or 2µM Methylstat. >30 cells analysed per condition, three independent experiments. **(L)** Graph showing the delta circularity (defined as the difference between nuclear circularity in G2 vs in G1) upon mitotic division (in grey) or MS (in blue) in RPE-1 cells treated with DMSO or 2µM Methylstat. Mean±SEM, >25 cells analysed per condition, three independent experiments. **(M-N)** Graphs showing **(M)** the nuclear circularity and solidity and **(N)** the H3K9me2 coefficient of variation at the NE in RPE-1 cells treated with DMSO or 4µM Methylstat. (M) >90 or (N) >40 G1 cells analysed per condition, three independent experiments. **(O)** Representative images displaying RPE-1 diploid and tetraploid cells treated with DMSO or with 4µM Methylstat. DNA in magenta. **(P-Q)** Graphs presenting nuclear circularity and solidity in **(P)** BJ or **(Q)** HCT116 cells treated with DMSO or 4µM Methylstat. Mean±SEM, >65 G1 cells analysed per condition, three independent experiments. **(R)** Representative images showing BJ (left panel) and HCT116 (right panel) diploid and tetraploid cells treated with DMSO or with 4µM Methylstat. DNA in magenta. Scale bars: 10µm. D=diploid; T=tetraploid; MS=mitotic slippage; NEBD= nuclear envelope breakdown; NE=nuclear envelope. (**B,E,J,K,L,M,N,P,Q**) Anova-test (one-sided). (**C,D,G,H**) t-test (two-sided). ns=not significant. *=P ≤ 0.05. **= P ≤ 0.01. ***= P ≤ 0.001. ****= P ≤ 0.0001.

Figure S7: Promoting H3K9 methylation prevents nuclear deformations upon MS

(A) Stills of time lapse movies showing RPE-1 cells stably expressing mCherry-H2B (in magenta) performing MS and treated with DMSO (upper panel) or 2µM Methylstat (lower panel). Microtubules were labelled using SPY650-Tubulin (in cyan). The white arrows indicate the microtubules transiently accumulating at the nuclear envelope. **(B)** Schematic workflow presenting the method used to treat cells with Methylstat before or after MS. **(C)** Super resolution representative images showing diploid and MS-generated tetraploid RPE-1 cells treated with DMSO or with 4µM Methylstat before and after MS. Lamin A/C in yellow hot, DNA in magenta. **(D-E)** Graph showing nuclear circularity and solidity in diploid and in MS-generated tetraploid cells (in grey and blue, respectively) treated with DMSO or with 4µM Methylstat. **(F-G)** Graph showing nuclear circularity and solidity in diploid and in MS-generated tetraploid cells (in grey and blue, respectively) treated with DMSO or with **(F)** GSK-J4 or **(G)** JIB. Mean±SEM, >70 G1 cells analysed per condition, three independent experiments. **(H)** Western blots of total protein extracts obtained from RPE-1 cells transfected with siCtrl or siPHF8 (upper panel) or overexpressing HA-G9a (lower panel). **(I-J)** Graphs showing nuclear circularity and solidity in diploid and in MS-generated tetraploid cells (in grey and blue, respectively) **(I)** transfected with siCtrl or siPHF8 or **(J)** overexpressing HA-G9a. Mean±SEM, >140 G1 cells analysed per condition, three independent experiments. **(K)** Schematic workflow presenting the method used to extend mitotic duration using Monastrol treatment. **(L)** Left panel – Super resolution representative images showing RPE-1 cells in prometaphase treated with DMSO or with 50µM Monastrol for 16hrs. H3S10 in green, DNA in magenta. Right panel – graph showing H3S10 mean intensity in early mitosis in RPE-1 diploid cells treated with DMSO or with 50µM Monastrol for 16hrs. Mean±SEM, >100 mitotic cells analysed, three independent experiments. **(M)** Graph showing nuclear circularity and solidity in diploid and in MS-generated tetraploid cells (in grey and blue, respectively) treated with DMSO or with 50µM Monastrol. Mean±SEM, >100 G1 cells analysed per condition, three independent experiments. **(N)** Representative images showing RPE-1 diploid cells treated with DMSO or with 5nM Calyculin. H3S10 and H3K9me2 in green and cyan hot, respectively, DNA in magenta. **(O)** Graph presenting nuclear circularity and solidity in RPE-1 diploid cells treated with DMSO or with 5nM Calyculin. Mean±SEM, >230 G1 cells analysed per condition, three independent experiments. Scale bars: 10µm. D=diploid; T=tetraploid; MS=mitotic slippage; ON=overnight. (**D,E,F,G,I,J,M**) Anova-test (one-sided). (**L,O,P**) t-test (two-sided). ns=not significant. *=P ≤ 0.05. **= P ≤ 0.01. ***= P ≤ 0.001. ****= P ≤ 0.0001.

Figure S8: Comparison of chromosome interactions in tetraploid and diploid RPE1 cells

(A) Graph showing the percentage of G1 diploid (in grey) and MS-generated tetraploid (in blue) RPE-1 cells before and after cell sorting. Mean ± SEM, >900 cells analysed, five independent experiments. **(B)** Representative images showing diploid and MS-generated tetraploid cells after cell sorting. DNA in magenta. **(C-D)** Boundary insulation scores for all **(C)** and top 300 most strongly insulating boundaries **(D)** between diploid (x-axis) and tetraploid (y-axis) conditions. *P* values were calculated using two-tailed Wilcoxon test. **(E)** Relationship between observed and expected intra-chromosomal values in tetraploid versus diploid. Each dot represents an inter-chromosomal interaction, red signifies higher and blue lower interaction signal in tetraploid compared to control. **(F)** Interactions alterations between chromatin sub-compartments between tetraploid and diploid cells. Blue suggests a loss of interaction, red a gain of interactions. *P* values were calculated using two-tailed Wilcoxon test. **(G-H)** Manhattan Plots of **(G)** H3K9me3- or **(H)** H3K9me2-enriched peaks density normalized in the tetraploid (up) and diploid (down) conditions by chromosomal arm and cytobands. **(I)** Karyoplots showing (left panel) H3K9me3 and (right panel) H3K9me2-enriched peaks density in the tetraploid (blue) and diploid (gray) condition across the genome. D=diploid; T=tetraploid; MS=mitotic slippage. ns=not significant. *=P ≤ 0.05. **= P ≤ 0.01. ***= P ≤ 0.001. ****= P ≤ 0.0001.

Figure S9: Physiological polyploid cells generated by cytokinesis failure and endoreplication exhibit homogenous nuclear shape

(A) Representative images presenting small and large MKs. DNA in magenta. **(B)** Graph showing nuclear area in HSCs and in MKs. The MK median nuclear area was used to distinguish small and large MKs. Mean±SEM, >150 interphase cells analysed per condition, three independent experiments. **(C)** Schematic workflow showing the methods used to obtain mouse hepatocytes. **(D)** Representative images showing diploid and polyploid hepatocytes. Actin in grey, DNA in magenta. **(E)** Super resolution representative images and their corresponding 3D reconstructions showing diploid and polyploid hepatocytes. Lamin A/C in yellow, DNA in magenta. **(F)** Schematic representation of *Drosophila* salivary glands. **(G)** Representative images and their corresponding 3D reconstructions showing polyploid salivary glands. Lamin A/C in yellow, DNA in magenta. **(H)** Representative immunofluorescence images showing *Drosophila* fat body (left panel) and ring gland (right panel). Lamin A/C or Nuclear pore complex (NPC) in yellow hot, Actin in grey, DNA in magenta. **(I-J)** Graph showing **(I)** the nuclear area and **(J)** the nuclear circularity and solidity index in diploid and in polyploid hepatocytes (in grey and yellow, respectively). The hepatocyte median nuclear area was used to distinguish small and large hepatocytes. Mean±SEM, >140 interphase cells analysed per condition, three independent experiments. **(K-L)** Graph showing **(K)** the nuclear area and **(L)** the nuclear circularity and solidity index in polyploid salivary glands at two different developmental stages (L2 and L3). Mean±SEM, **(K)** >100 and **(L)** >60 cells analysed, three independent experiments. Scale bars: 10µm. D=diploid; P=polyploid; HSC=hematopoietic stem cell; MK=megakaryocyte. NPC=Nuclear pore complex. (**B,I,J,K,L**) t-test (two-sided). ns=not significant. *=P ≤ 0.05. **= P ≤ 0.01. ***= P ≤ 0.001. ****= P ≤ 0.0001.

Figure S10: Hepatocytes and salivary gland cells do no exhibit defects in H3K9me2 and Lamin A/C distribution upon polyploidization

(A-B) Left panel – Graph showing line scan measurements of microtubules and DNA fluorescence intensities close to the NE in **(B)** hepatocytes and **(C)** salivary gland cells measured in the cells presented in the right panels. Right panel - representative images showing the microtubule cytoskeleton in **(B)** hepatocytes and **(C)** salivary gland cells. Microtubules in cyan, DNA in magenta. **(C)** Super resolution representative images showing diploid HSC and polyploid megakaryocytes. H3K27ac in cyan hot, DNA in magenta. **(D)** Graph showing H3K27ac mean intensity in HSCs and in megakaryocytes (in grey and blue, respectively). Mean±SEM, >200 cells analysed, three independent experiments. **(E)** Super resolution representative images showing diploid and polyploid hepatocytes. Lamin A/C and H3K9me2 in yellow hot and cyan hot, respectively, DNA in magenta. **(F-G)** Graphs showing **(F)** the relative H3K9me2 mean intensity at the NE and **(G)** the H3K9me2 coefficient of variation (define as the ratio of the standard deviation to the mean) at the NE in diploid (in grey) and in polyploid (in yellow) hepatocytes. Mean±SEM, >90 interphase cells analysed per condition, three independent experiments. **(H)** Representative images showing diploid and hepatocytes. DNA in magenta. **(I)** Super resolution representative images showing diploid and polyploid hepatocytes. Lamin A/C and Lamin in yellow hot and red hot, respectively, DNA in magenta. **(J-L)** Graph presenting **(J)** Lamin A/C and **(K)** Lamin B1 mean intensity at the NE and **(L)** the Lamin B1 vs Lamin A/C ratio at the NE in hepatocytes. Mean±SEM, >90 interphase cells analysed per condition, three independent experiments. **(M-N)** Graphs showing **(M)** Lamin A/C and **(N)** Lamin B1 mean intensity at the NE in *Drosophila* salivary glands. Mean±SEM, >150 cells analysed per condition, three independent experiments. **(O)** Representative images showing *Drosophila* salivary glands at two different developmental stages (L2 and L3). Lamin A/C and Lamin B1 in yellow hot and red hot, respectively, Actin in grey, DNA in magenta. **(P)** Graph showing the mean H3K9me2 intensity in interphase in small megakaryocytes treated with DMSO or with 4µM Methylstat. Mean±SEM, >110 cells analysed, three independent experiments. Scale bars: 10µm. D=diploid; P=polyploid; HC=hepatocytes; HSC=Hematopoietic stem cells; MK=megakaryocytes; NE=nuclear envelope. (**D**) Anova-test (one-sided). (**F,G,J,K,L,M,N,P**) t-test (two-sided). ns=not significant. *=P ≤ 0.05. **= P ≤ 0.01. ***= P ≤ 0.001. ****= P ≤ 0.0001.

Videos 1 and 2: Mitotic slippage generated tetraploid cells with nuclear deformations.
Time lapse videos of RPE-1 cells expressing mCherry-H2B (in magenta) and performing canonical mitosis (video 1) or mitotic slippage (video 2). Images were acquired every 5 minutes.

Videos 3 and 4: Microtubules, but not actin, accumulate around nuclear deformations upon mitotic slippage.
Time lapse videos of RPE-1 cells expressing mCherry-H2B (in magenta) performing mitotic slippage. Microtubules were labeled using SPY Tubulin (in Cyan, video 3) and actin was labeled using SPY FAST Actin (in blue, video 4). Images were acquired every 3 minutes.

Videos 5 and 6: Microtubule depolymerization prevents nuclear deformations upon mitotic slippage.
Time lapse videos of RPE-1 cells expressing mCherry-H2B (in magenta) and performing mitotic slippage in the absence (video 5) or presence of Nocodazole (video 6). Microtubules were labeled using SPY Tubulin (in Cyan). Images were acquired every 3 minutes.

Videos 7 and 8: Microtubule depolymerization prevents nuclear deformations upon mitotic slippage induced by CCNB1 depletion.
Time lapse videos of RPE-1 CCNB1 cells expressing mCherry-H2B (in magenta) and performing mitotic slippage in the absence (video 7) or presence of Nocodazole (video 8). Microtubules were labeled using SPY Tubulin (in Cyan). Images were acquired every 3 minutes.

Video 9: Decreasing H3S10 phosphorylation prevents nuclear deformations upon mitotic slippage.
Time lapse videos of RPE-1 CCNB1 cells expressing mCherry-H2B (in magenta) and performing mitotic slippage in the presence of Methylstat. Microtubules were labeled using SPY Tubulin (in Cyan). Images were acquired every 5 minutes.

Videos 10 and 11: Megakaryocytes become polyploid by mitotic slippage.
Time lapse videos Megakaryocytes expressing mCherry-H2B (in magenta) and performing mitotic slippage. Images were acquired every 10 minutes.

Figure 1

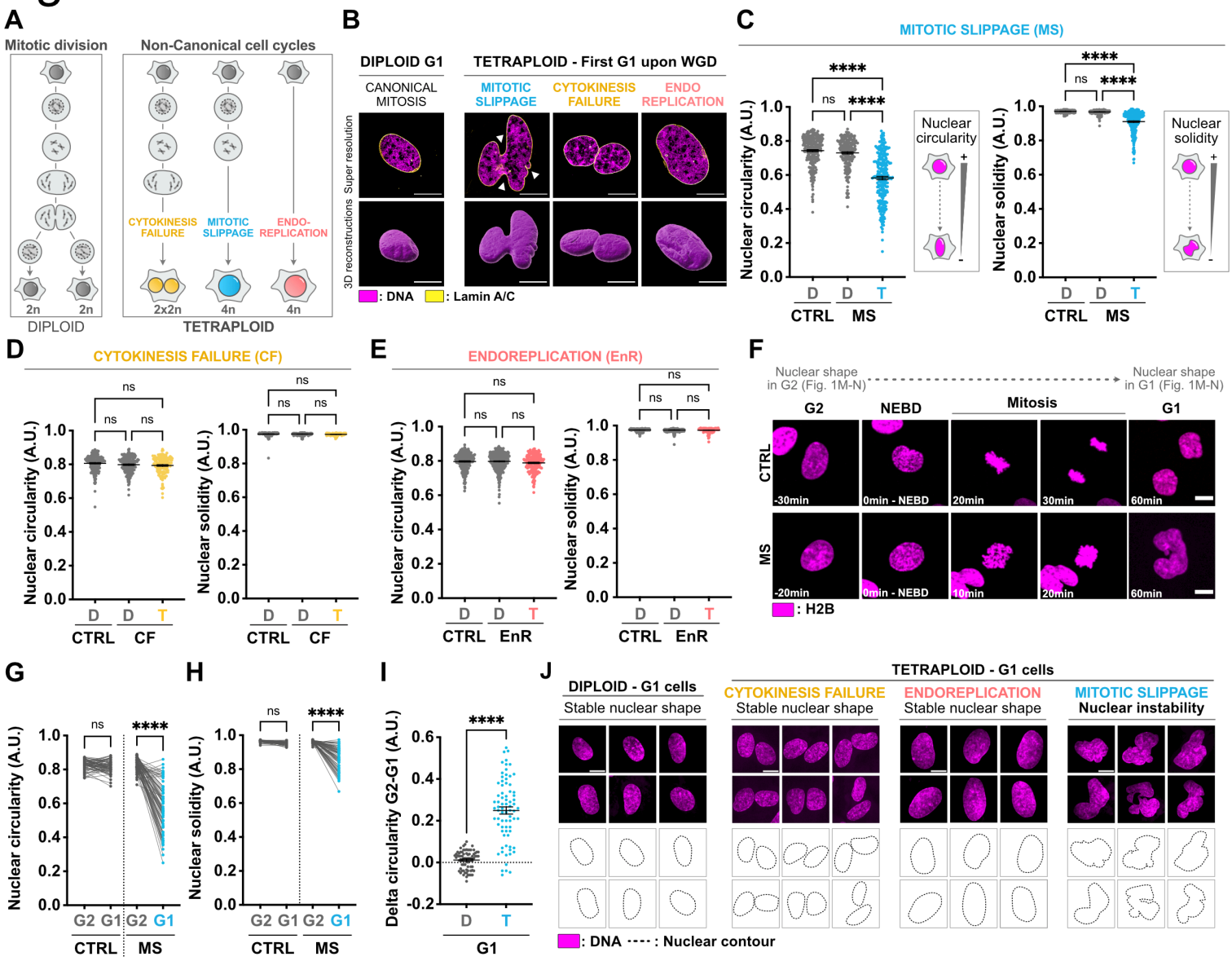
A
Mitotic division
Non-Canonical cell cycles
CYTOKINESIS FAILURE
MITOTIC SLIPPAGE
ENDO-REPLICATION
2n
2n
2x2n
4n
4n
DIPLOID
TETRAPLOID
B
DIPLOID G1
TETRAPLOID - First G1 upon WGD
CANONICAL MITOSIS
MITOTIC SLIPPAGE
CYTOKINESIS FAILURE
ENDO REPLICATION
Super resolution
3D reconstructions
: DNA
: Lamin A/C
C
MITOTIC SLIPPAGE (MS)
Nuclear circularity (A.U.)
Nuclear solidity (A.U.)
Nuclear circularity
Nuclear solidity
CTRL
MS
D
T
ns
****
D
CYTOKINESIS FAILURE (CF)
CF
E
ENDOREPLICATION (EnR)
EnR
F
Nuclear shape in G2 (Fig. 1M-N)
Nuclear shape in G1 (Fig. 1M-N)
G2
NEBD
Mitosis
G1
CTRL
MS
-30min
0min - NEBD
20min
30min
60min
-20min
10min
: H2B
G
H
I
Delta circularity G2-G1 (A.U.)
G2 G1 G2 G1
J
DIPLOID - G1 cells
TETRAPLOID - G1 cells
Stable nuclear shape
CYTOKINESIS FAILURE
ENDOREPLICATION
MITOTIC SLIPPAGE
Nuclear instability
: DNA
: Nuclear contour

Figure 2

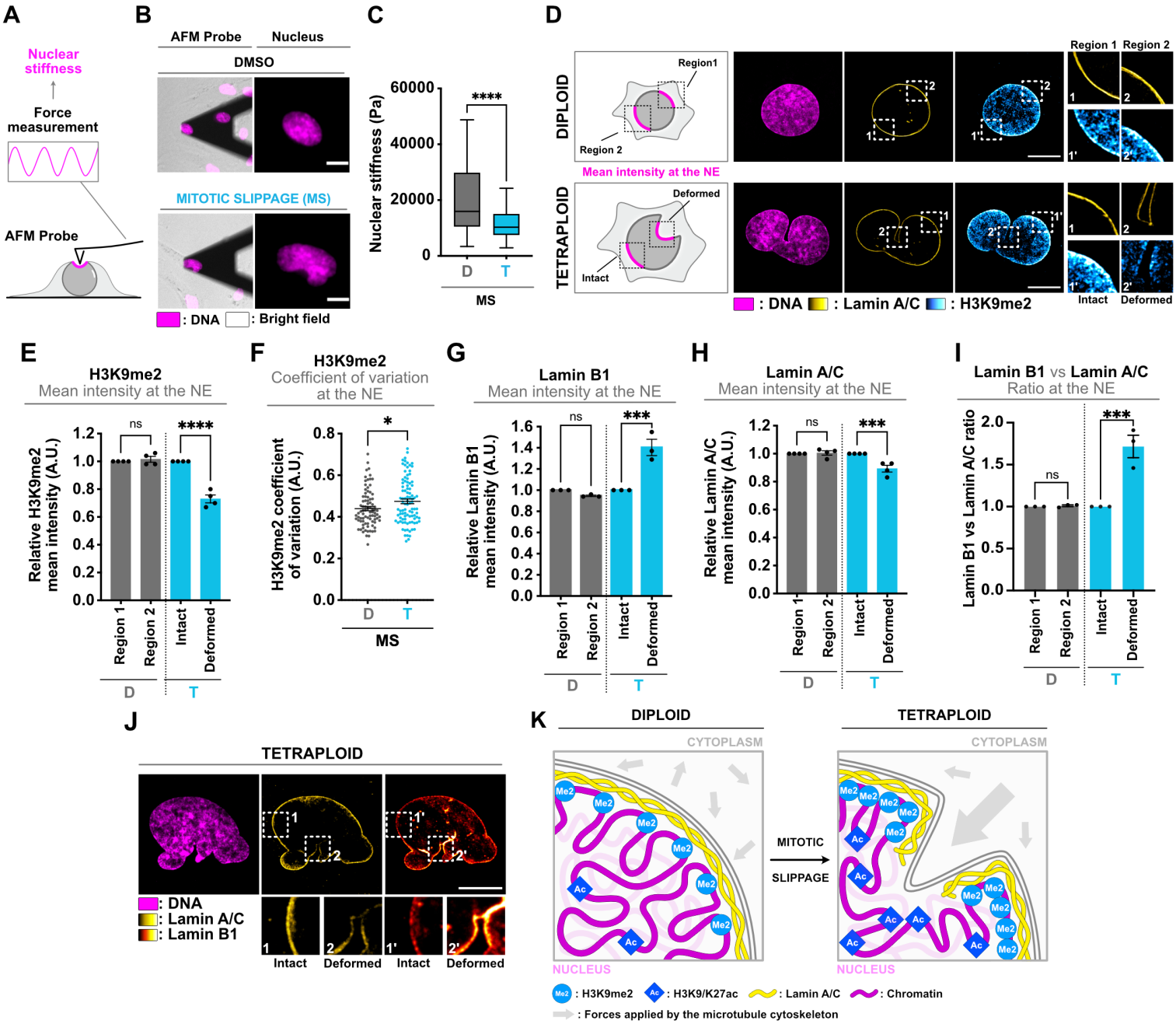
A
Nuclear stiffness
Force measurement
AFM Probe
B
AFM Probe
Nucleus
DMSO
MITOTIC SLIPPAGE (MS)
: DNA
: Bright field
C
Nuclear stiffness (Pa)
60000
40000
20000
0
****
D
T
MS
D
DIPLOID
Region1
Region 2
Mean intensity at the NE
TETRAPLOID
Deformed
Intact
Region 1
Region 2
: DNA
: Lamin A/C
: H3K9me2
Intact
Deformed
E
H3K9me2
Mean intensity at the NE
Relative H3K9me2 mean intensity (A.U.)
ns
****
Region 1
Region 2
Intact
Deformed
D
T
F
H3K9me2
Coefficient of variation at the NE
H3K9me2 coefficient of variation (A.U.)
*
D
T
MS
G
Lamin B1
Mean intensity at the NE
Relative Lamin B1 mean intensity (A.U.)
ns
***
Region 1
Region 2
Intact
Deformed
D
T
H
Lamin A/C
Mean intensity at the NE
Relative Lamin A/C mean intensity (A.U.)
ns
***
Region 1
Region 2
Intact
Deformed
D
T
I
Lamin B1 vs Lamin A/C
Ratio at the NE
Lamin B1 vs Lamin A/C ratio
ns
***
Region 1
Region 2
Intact
Deformed
D
T
J
TETRAPLOID
: DNA
: Lamin A/C
: Lamin B1
Intact
Deformed
Intact
Deformed
K
DIPLOID
TETRAPLOID
CYTOPLASM
NUCLEUS
MITOTIC
SLIPPAGE
Me2
Ac
: H3K9me2
: H3K9/K27ac
: Lamin A/C
: Chromatin
: Forces applied by the microtubule cytoskeleton

Figure 3

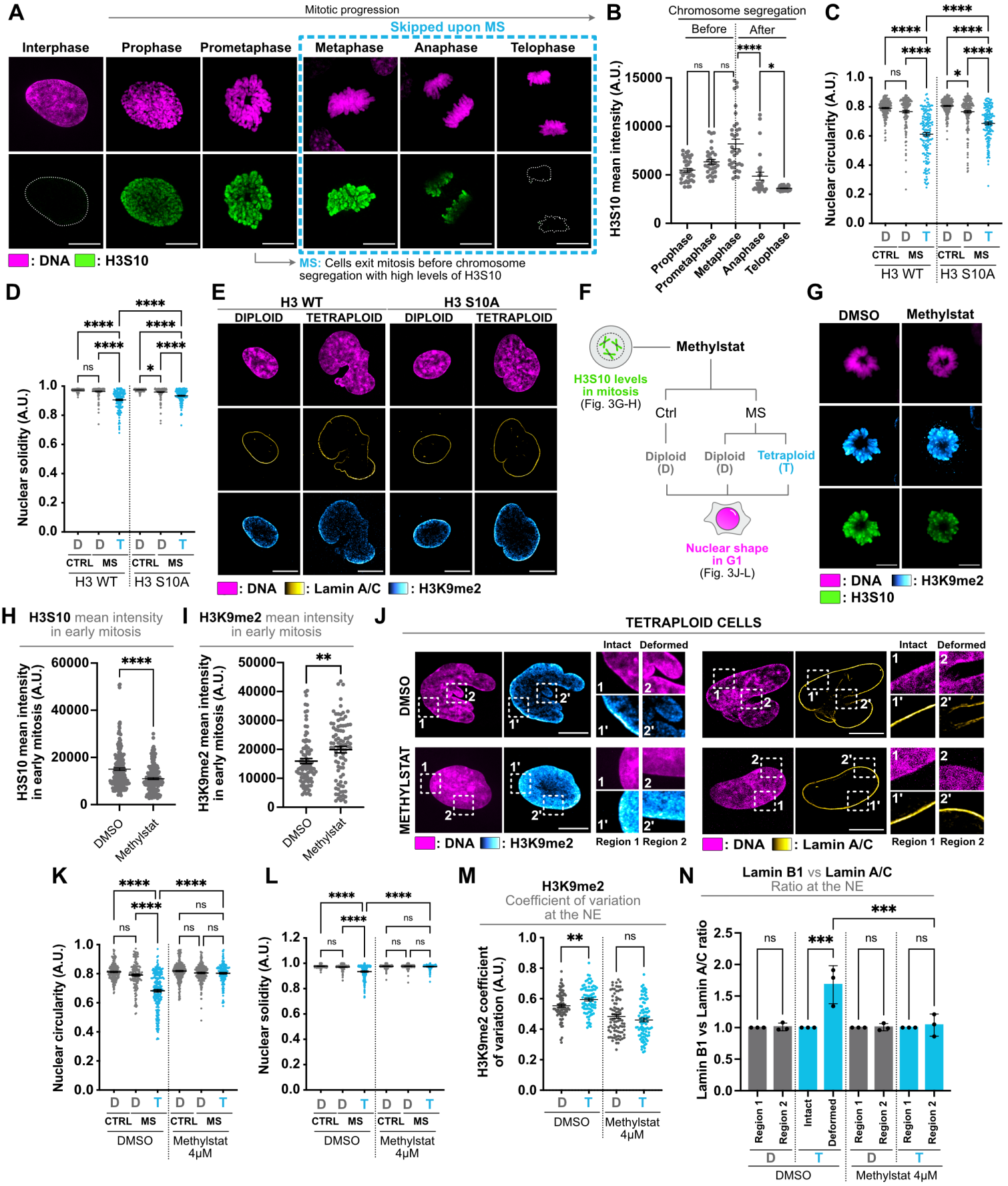
A
Mitotic progression
Skipped upon MS
Interphase
Prophase
Prometaphase
Metaphase
Anaphase
Telophase
: DNA
: H3S10
MS: Cells exit mitosis before chromosome segregation with high levels of H3S10
B
Chromosome segregation
Before
After
H3S10 mean intensity (A.U.)
Prophase
Prometaphase
Metaphase
Anaphase
Telophase
C
Nuclear circularity (A.U.)
CTRL
MS
H3 WT
H3 S10A
D
Nuclear solidity (A.U.)
E
H3 WT
H3 S10A
DIPLOID
TETRAPLOID
: DNA
: Lamin A/C
: H3K9me2
F
Methylstat
H3S10 levels in mitosis (Fig. 3G-H)
Ctrl
MS
Diploid (D)
Diploid (D)
Tetraploid (T)
Nuclear shape in G1 (Fig. 3J-L)
G
DMSO
Methylstat
: DNA
: H3K9me2
: H3S10
H
H3S10 mean intensity in early mitosis
H3S10 mean intensity in early mitosis (A.U.)
DMSO
Methylstat
I
H3K9me2 mean intensity in early mitosis
H3K9me2 mean intensity in early mitosis (A.U.)
J
TETRAPLOID CELLS
Intact
Deformed
DMSO
METHYLSTAT
: DNA
: H3K9me2
Region 1
Region 2
: Lamin A/C
K
Nuclear circularity (A.U.)
DMSO
Methylstat 4μM
L
Nuclear solidity (A.U.)
M
H3K9me2
Coefficient of variation at the NE
H3K9me2 coefficient of variation (A.U.)
N
Lamin B1 vs Lamin A/C
Ratio at the NE
Lamin B1 vs Lamin A/C ratio
Methylstat 4μM

Figure 4

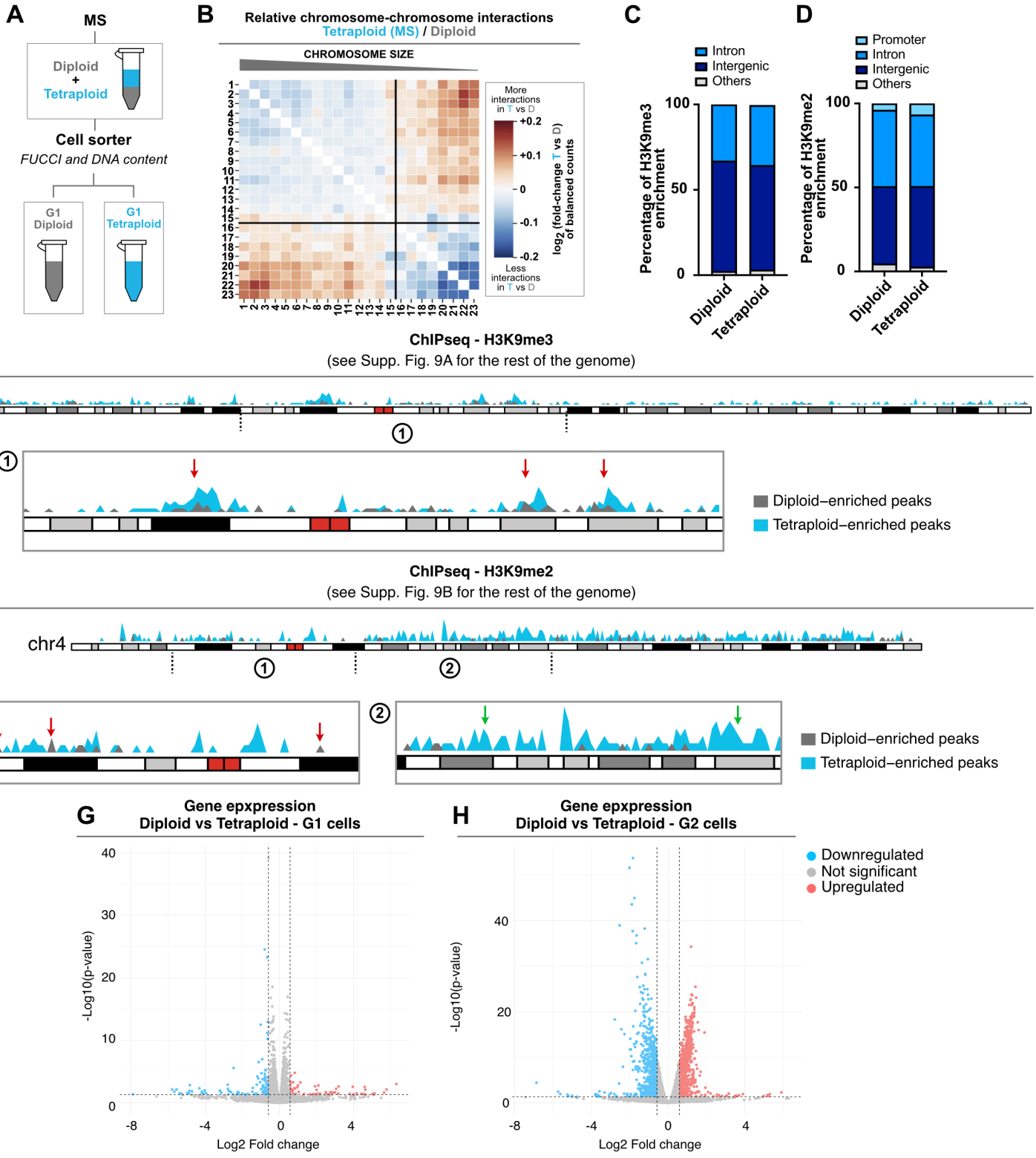
A
MS
Diploid
+
Tetraploid
Cell sorter
FUCCI and DNA content
G1
Diploid
G1
Tetraploid
B
Relative chromosome-chromosome interactions
Tetraploid (MS) / Diploid
CHROMOSOME SIZE
More interactions in T vs D
Less interactions in T vs D
log2 (fold-change T vs D) of balanced counts
C
Intron
Intergenic
Others
Percentage of H3K9me3 enrichment
Diploid
Tetraploid
D
Promoter
Intron
Intergenic
Others
Percentage of H3K9me2 enrichment
Diploid
Tetraploid
E
ChIPseq - H3K9me3
(see Supp. Fig. 9A for the rest of the genome)
chr2
Diploid–enriched peaks
Tetraploid–enriched peaks
F
ChIPseq - H3K9me2
(see Supp. Fig. 9B for the rest of the genome)
chr4
Diploid–enriched peaks
Tetraploid–enriched peaks
G
Gene epxpression
Diploid vs Tetraploid - G1 cells
-Log10(p-value)
Log2 Fold change
H
Gene epxpression
Diploid vs Tetraploid - G2 cells
-Log10(p-value)
Log2 Fold change
Downregulated
Not significant
Upregulated

Figure 5

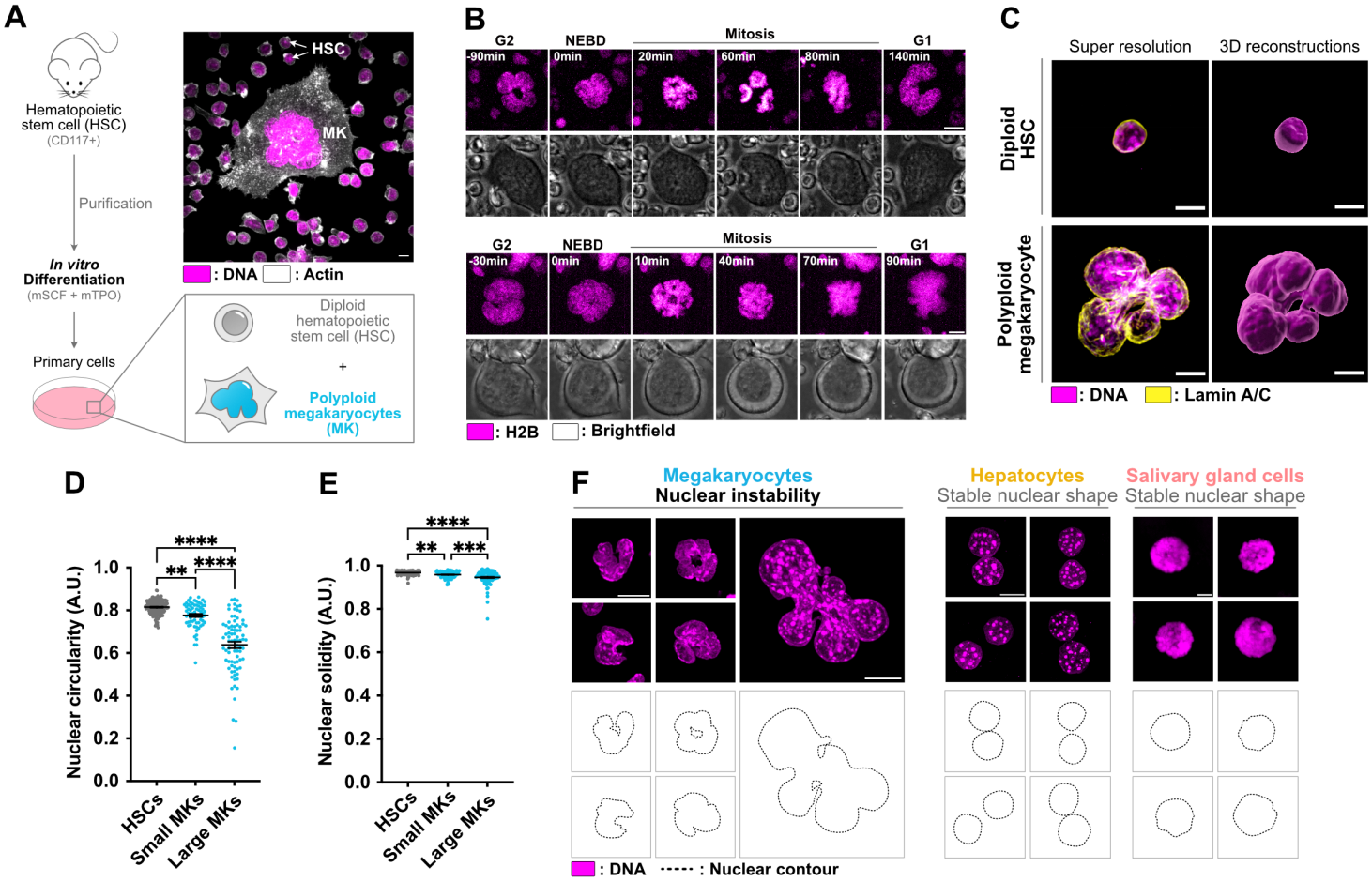
A
Hematopoietic stem cell (HSC)
(CD117+)
Purification
In vitro Differentiation
(mSCF + mTPO)
Primary cells
HSC
MK
: DNA
: Actin
Diploid hematopoietic stem cell (HSC)
+
Polyploid megakaryocytes (MK)
B
G2
NEBD
Mitosis
G1
-90min
0min
20min
60min
80min
140min
-30min
10min
40min
70min
90min
: H2B
: Brightfield
C
Super resolution
3D reconstructions
Diploid HSC
Polyploid megakaryocyte
: DNA
: Lamin A/C
D
Nuclear circularity (A.U.)
HSCs
Small MKs
Large MKs
E
Nuclear solidity (A.U.)
F
Megakaryocytes
Nuclear instability
Hepatocytes
Stable nuclear shape
Salivary gland cells
Stable nuclear shape
: DNA
: Nuclear contour

Figure 6

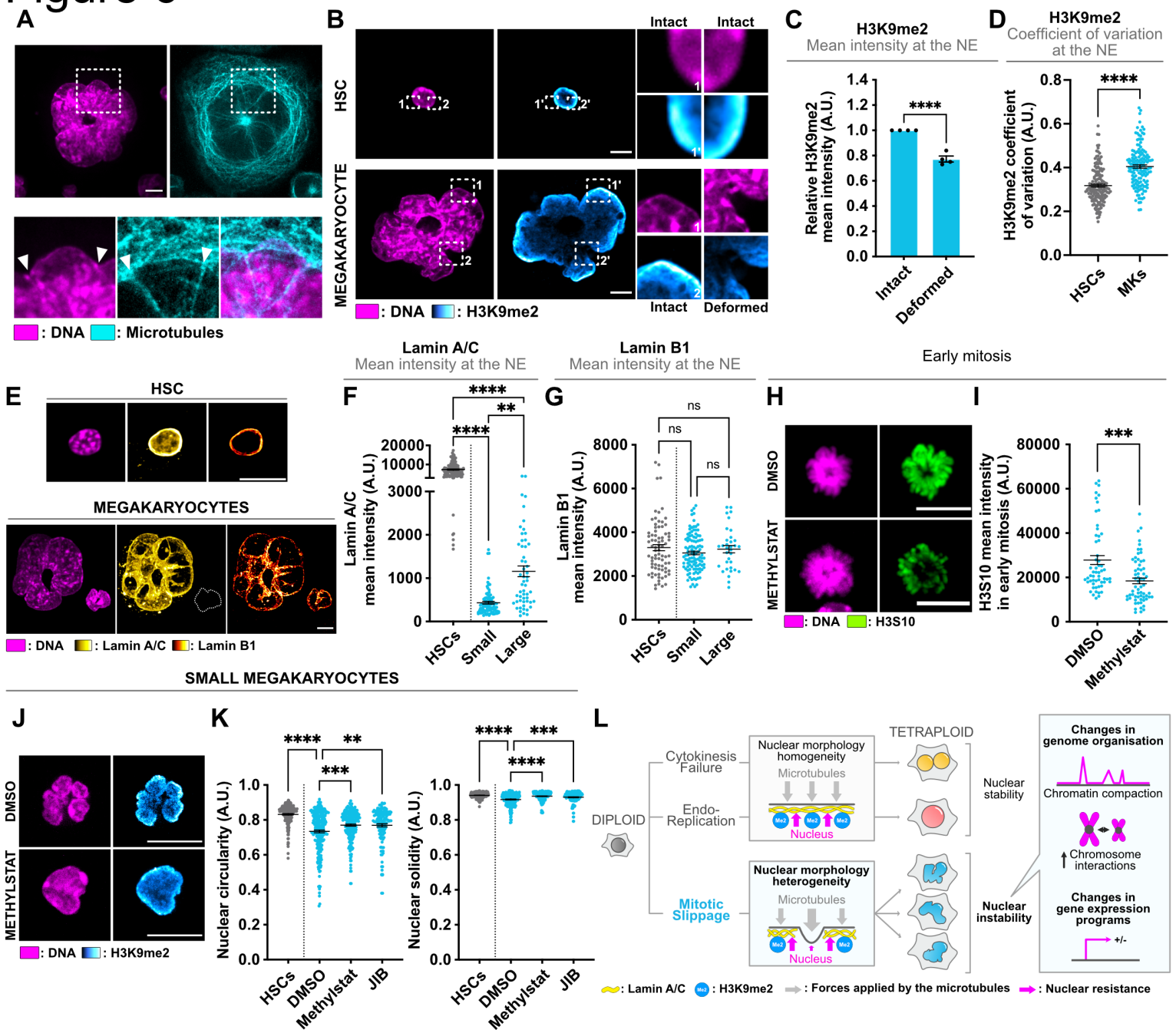
A
: DNA
: Microtubules
B
HSC
MEGAKARYOCYTE
Intact
Intact
Intact
Deformed
: DNA
: H3K9me2
C
H3K9me2
Mean intensity at the NE
Relative H3K9me2 mean intensity (A.U.)
****
Intact
Deformed
D
H3K9me2
Coefficient of variation at the NE
H3K9me2 coefficient of variation (A.U.)
****
HSCs
MKs
E
HSC
MEGAKARYOCYTES
: DNA
: Lamin A/C
: Lamin B1
Lamin A/C
Mean intensity at the NE
F
Lamin A/C mean intensity (A.U.)
****
**
****
HSCs
Small
Large
Lamin B1
Mean intensity at the NE
G
Lamin B1 mean intensity (A.U.)
ns
ns
ns
HSCs
Small
Large
Early mitosis
H
DMSO
METHYLSTAT
: DNA
: H3S10
I
H3S10 mean intensity in early mitosis (A.U.)
***
DMSO
Methylstat
SMALL MEGAKARYOCYTES
J
DMSO
METHYLSTAT
: DNA
: H3K9me2
K
Nuclear circularity (A.U.)
****
**
***
Nuclear solidity (A.U.)
****
***
****
HSCs
DMSO
Methylstat
JIB
L
DIPLOID
Cytokinesis Failure
Endo-Replication
Mitotic Slippage
Nuclear morphology homogeneity
Microtubules
Nucleus
Nuclear morphology heterogeneity
Microtubules
Nucleus
TETRAPLOID
Nuclear stability
Nuclear instability
Changes in genome organisation
Chromatin compaction
Chromosome interactions
Changes in gene expression programs
+/-
: Lamin A/C
: H3K9me2
: Forces applied by the microtubules
: Nuclear resistance

Supp Figure 1

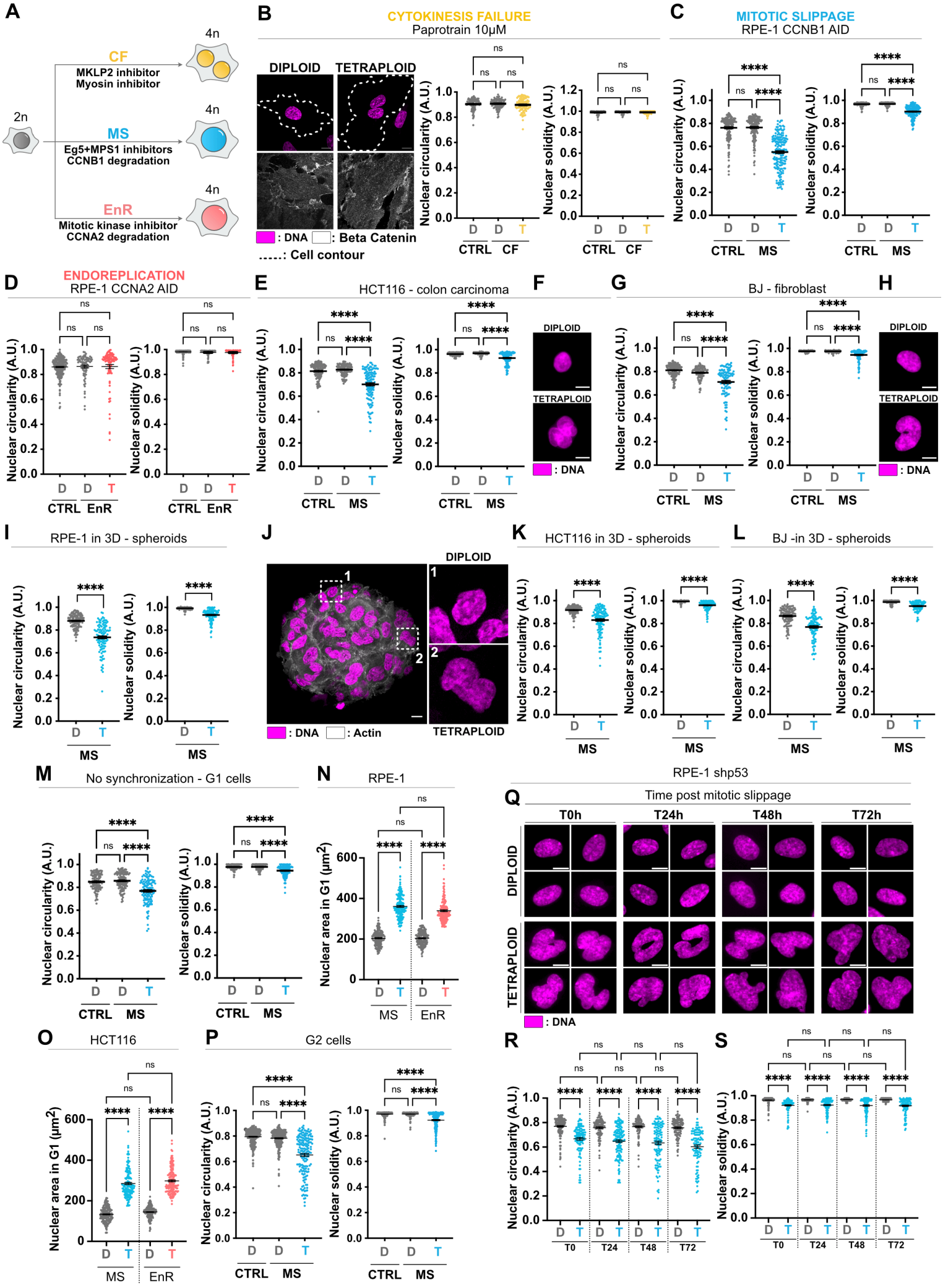

Supp Figure 2

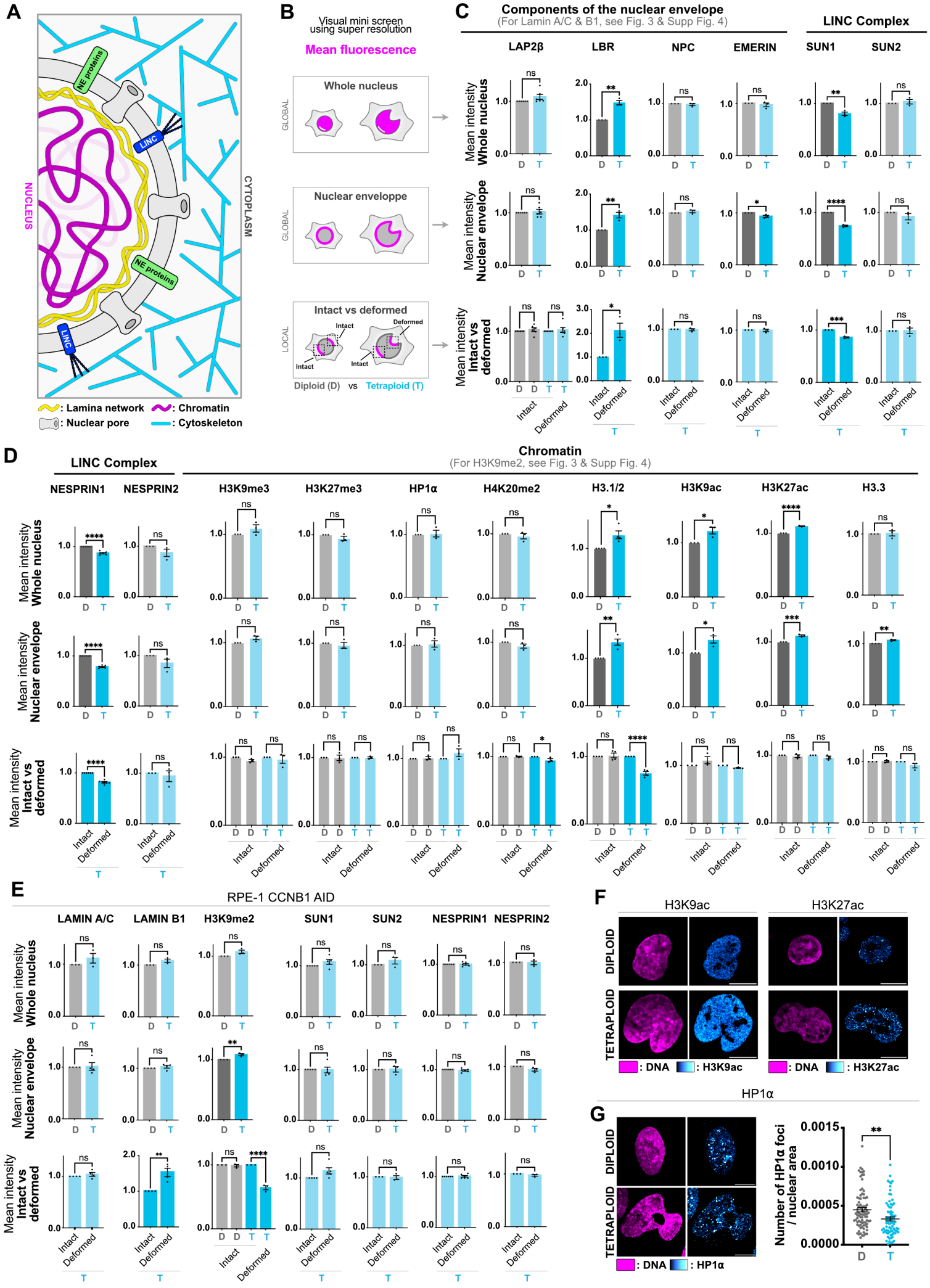

Supp Figure 3

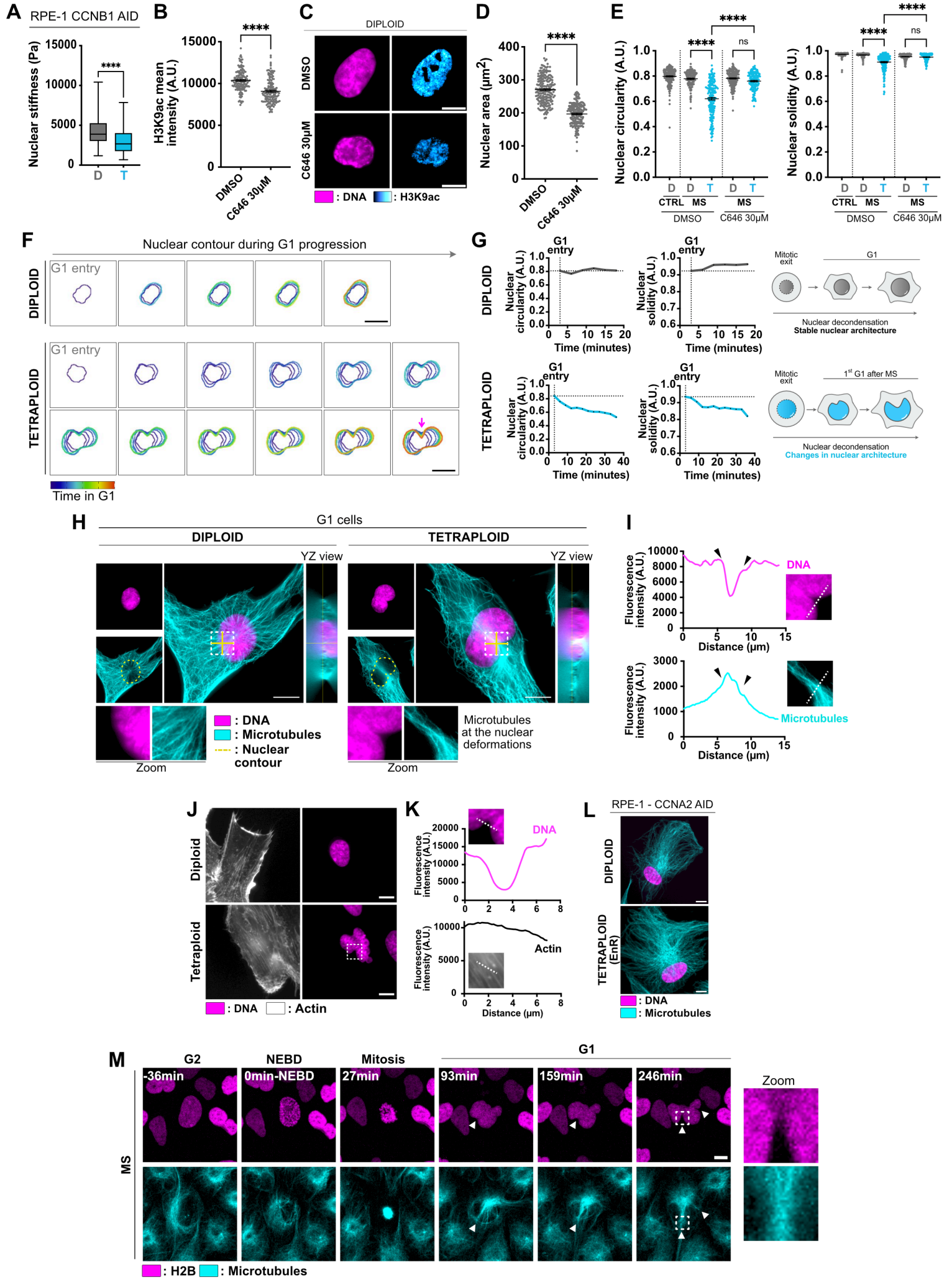

Supp Figure 4

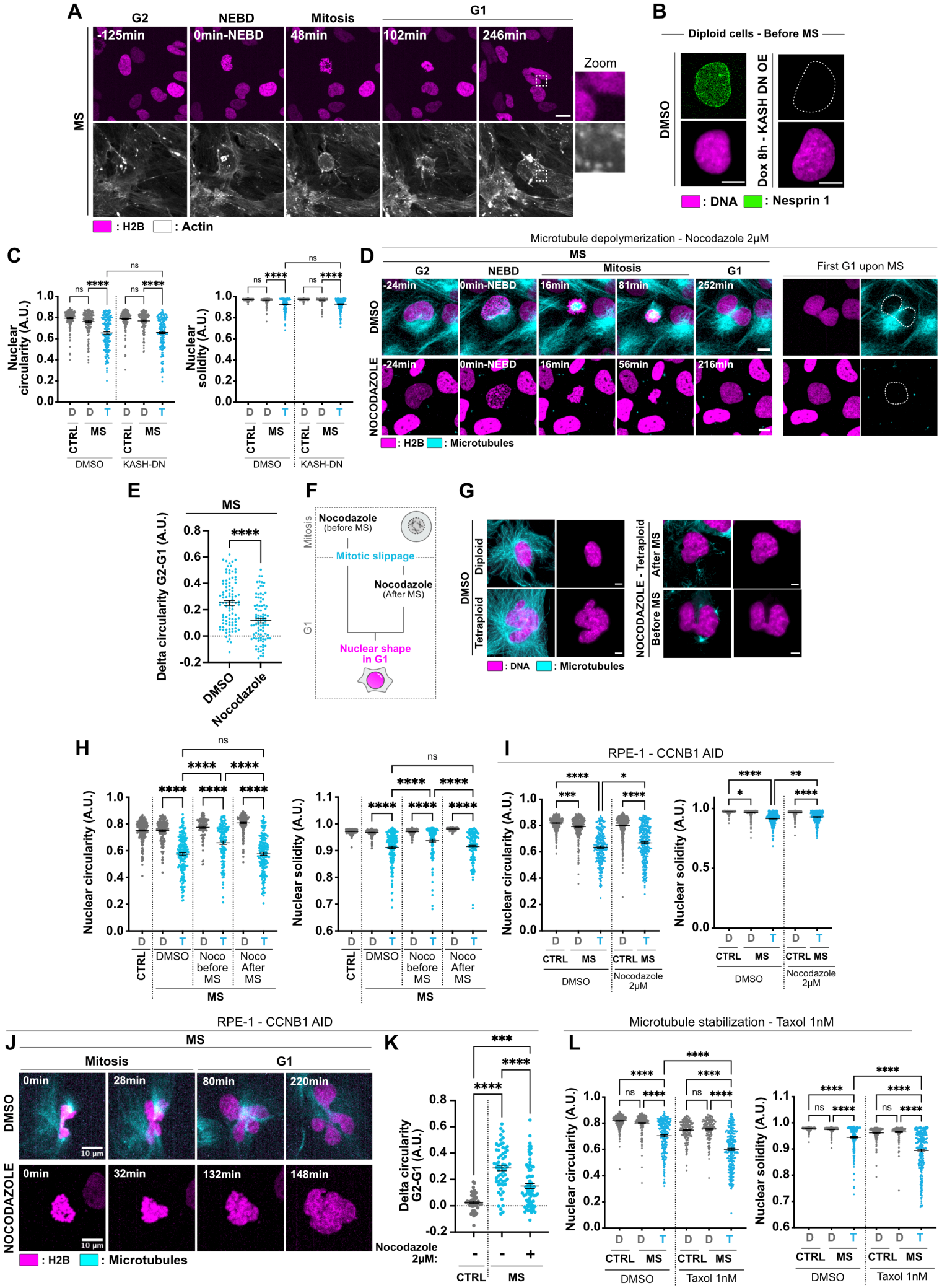

Supp Figure 5

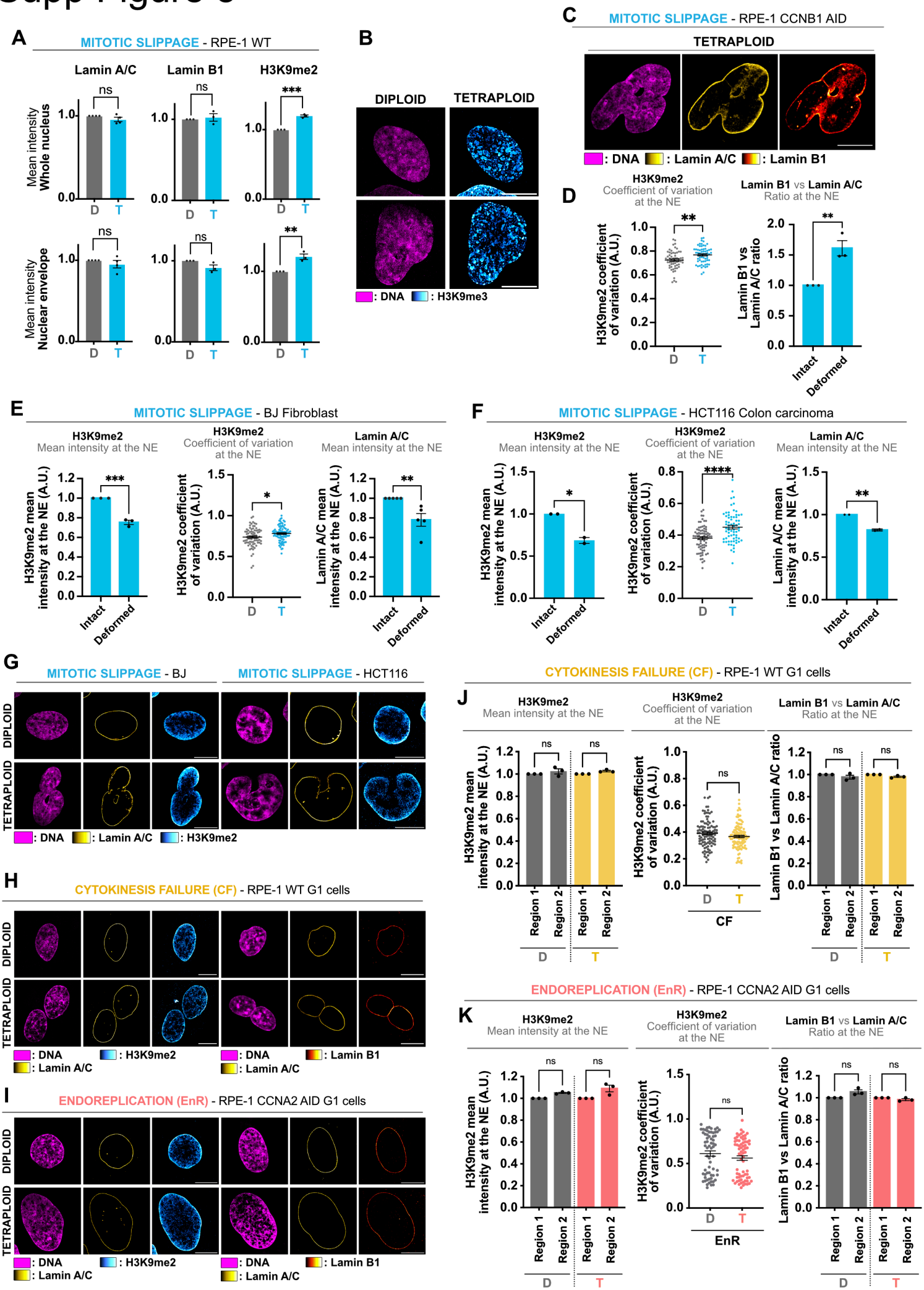

Supp Figure 6

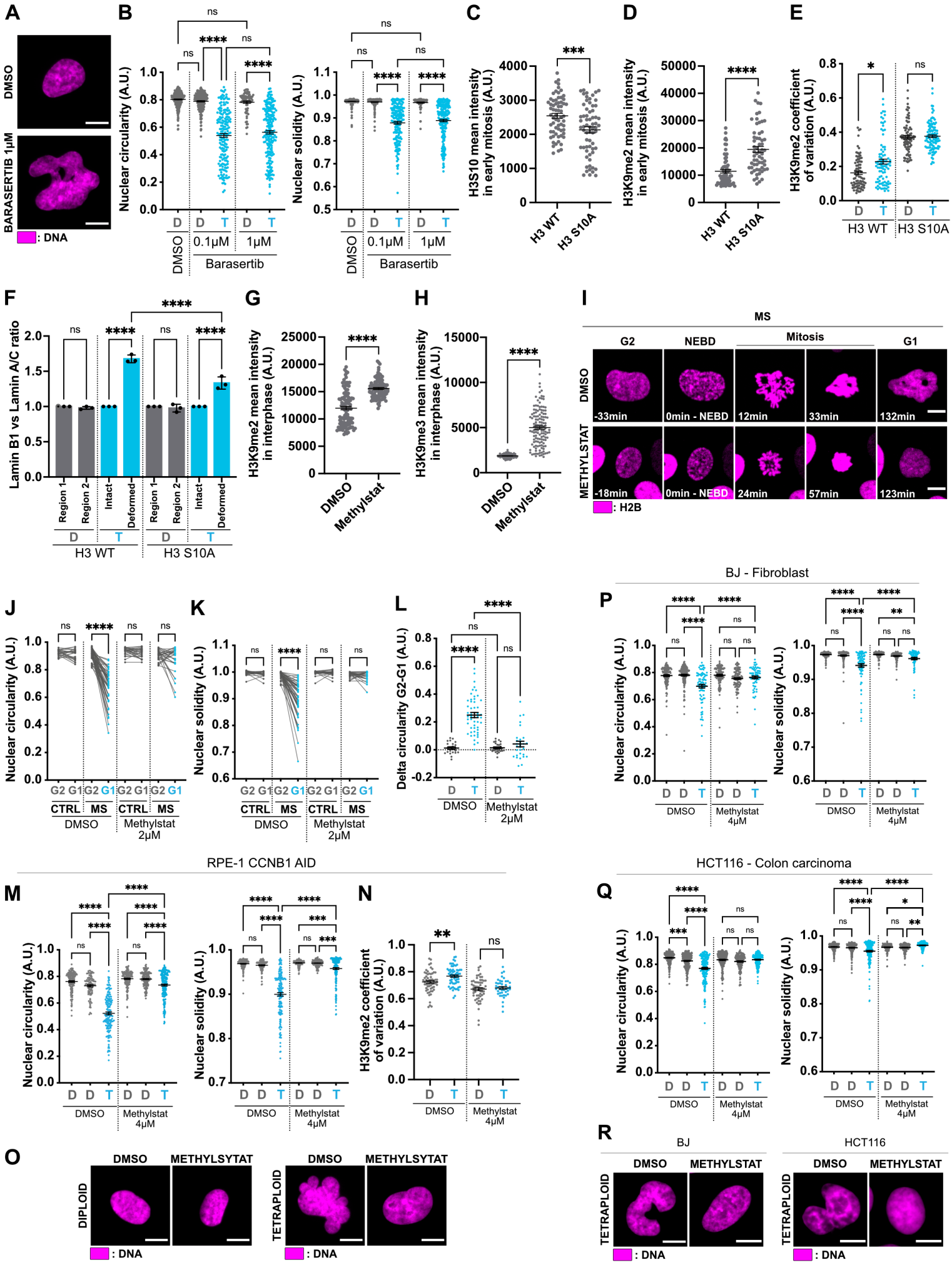

Supp Figure 7

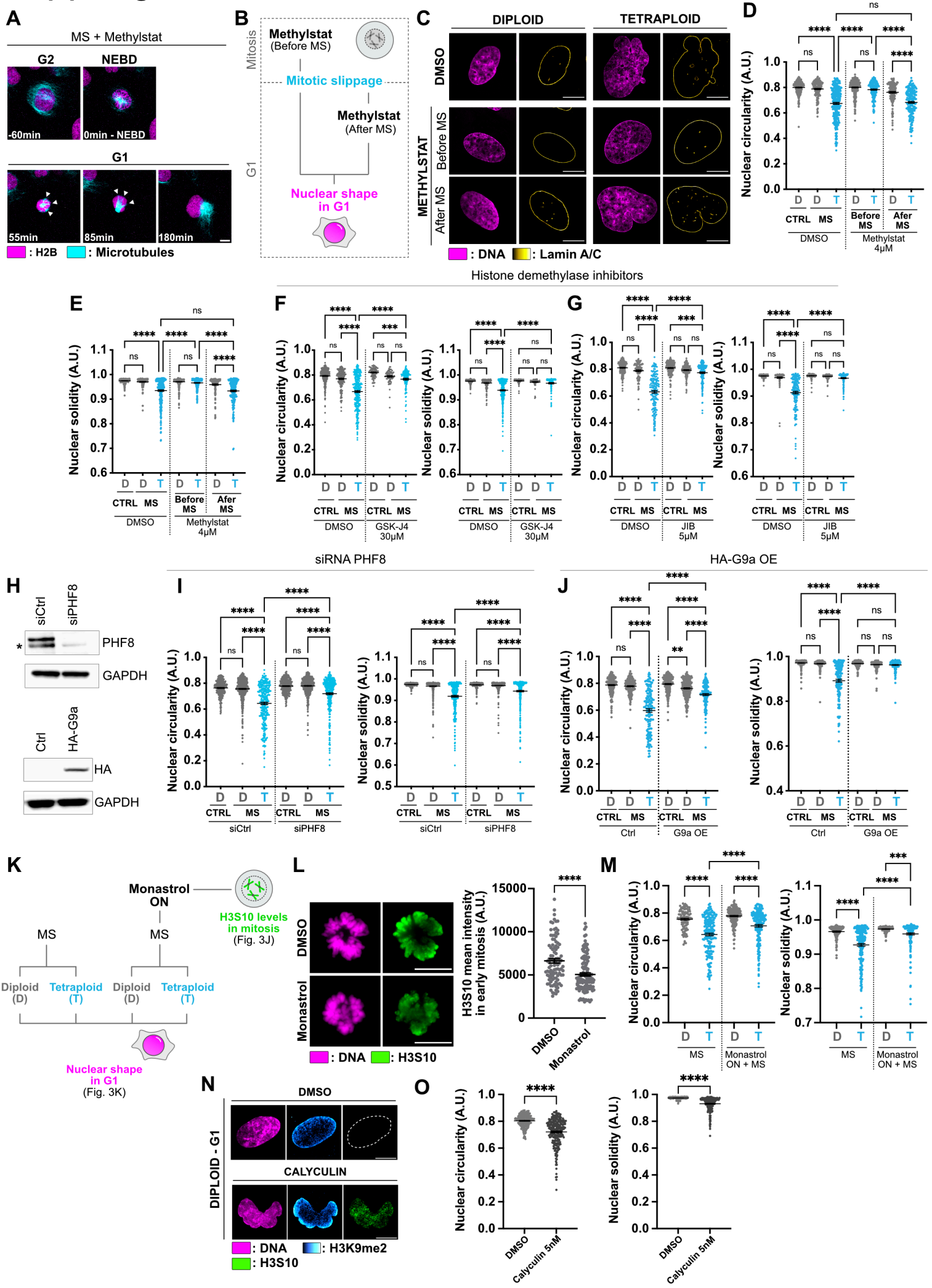

Supp Figure 8

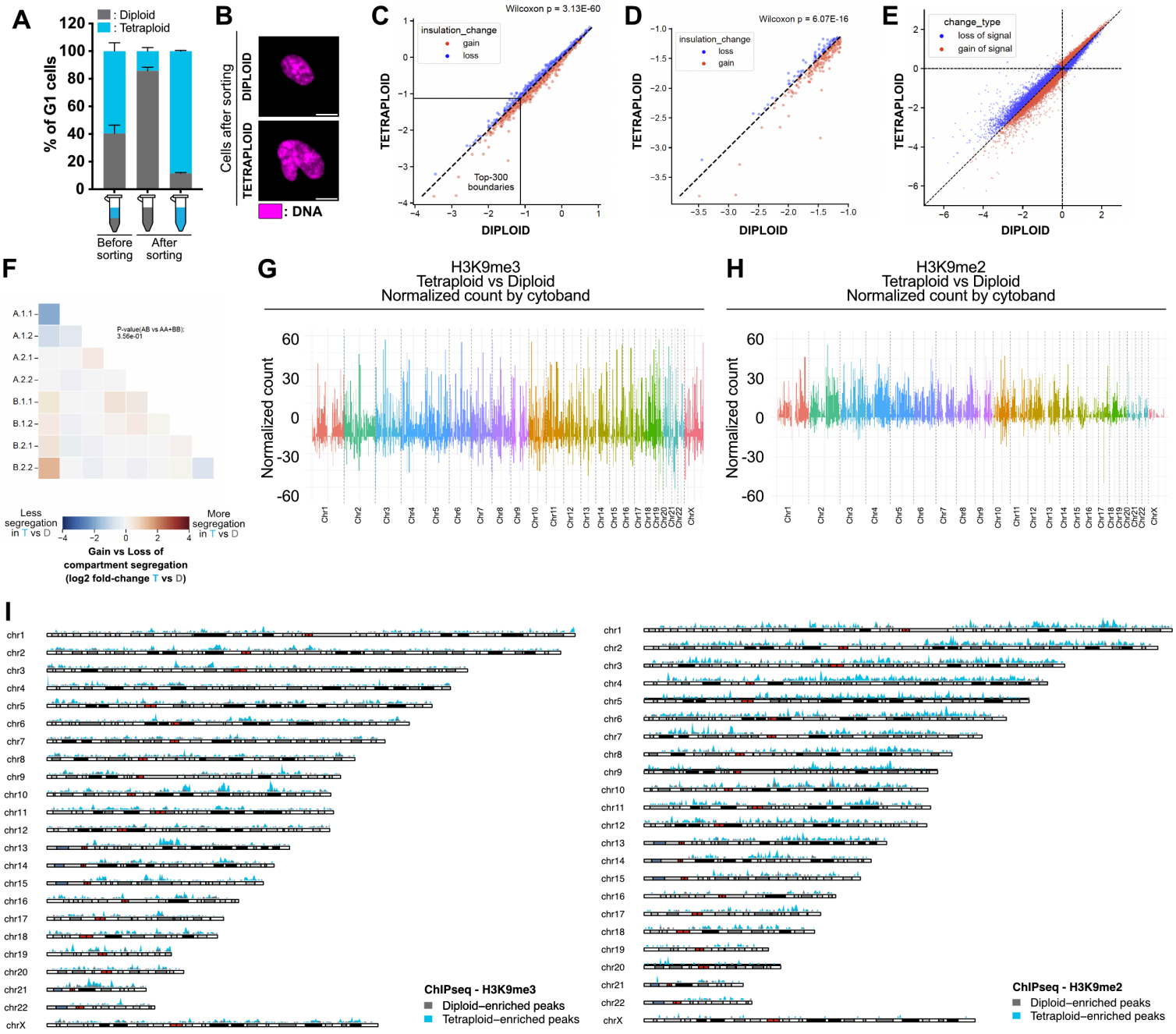

Supp Figure 9

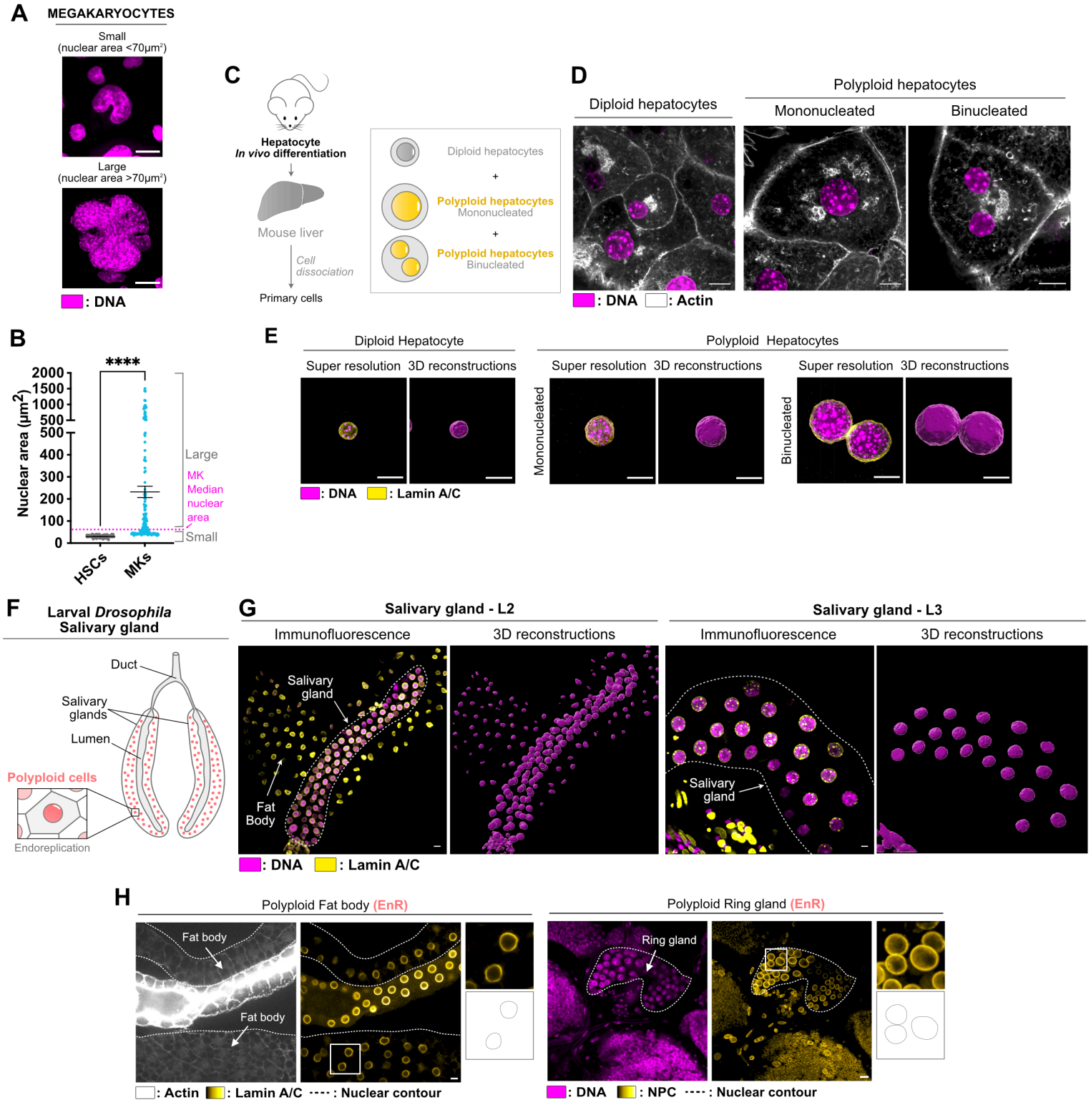
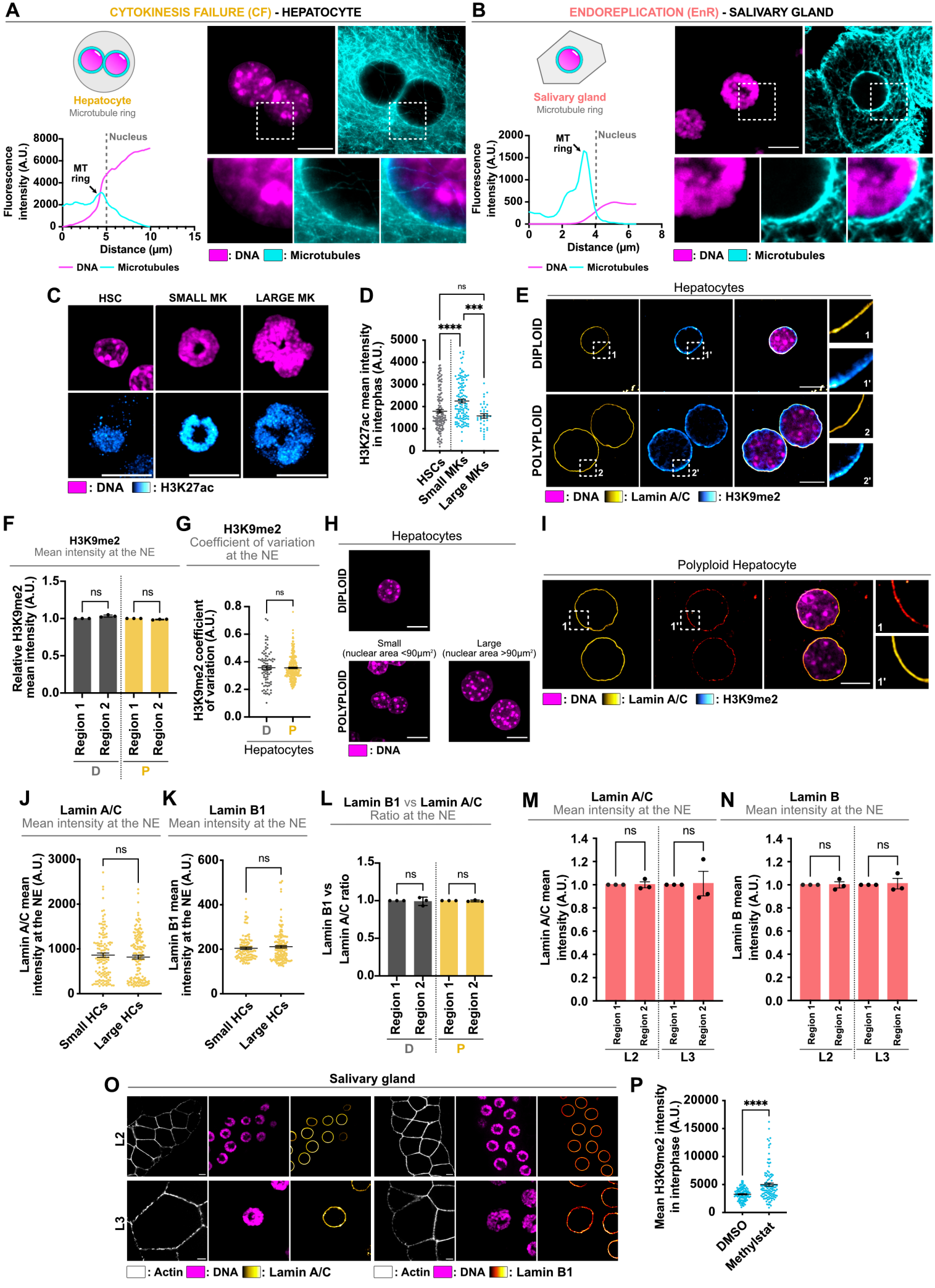
Supp Figure 10